Skeletal Muscle Proteostasis Promotes Central Nervous System Function and Reduces Neuroinflammation during Aging and Neurodegenerative Disease

Ian Matthews [1,2]

Allison Birnbaum [1,2]

Anastasia Gromova [3]

Kristen Coutinho [5]

Megan McGraw [6]

Dalton C. Patterson [6]

Macy T. Banks [6]

Amber Nobles [7]

Nhat Nguyen [3]

Helen C. Miranda [8-10]

Albert R. La Spada [3,4] (co-corresponding author)

Constanza J. Cortes [1,2](corresponding author)

[1] Leonard Davis School of Gerontology, [2] University of Southern California, [3] Department of Pathology and Laboratory Medicine, University of California, Irvine, [4] Department of Neurology and Department of Biological Chemistry, UCI Institute for Neurotherapeutics, University of California, Irvine, [5] Comprehensive Diabetes Center, University of Alabama at Birmingham, [6] Department of Cell, Developmental and Integrative Biology, University of Alabama at Birmingham, [7] Department of Neurology, University of Alabama at Birmingham, [8] Department of Genetics and Genome Sciences, School of Medicine, Case Western University, [9] Department of Neurosciences, School of Medicine, Case Western Reserve University, [10] RNA Center, School of Medicine, Case Western Reserve University,

Funding: NIH R01 AG077536 (CJC), University of Washington Nathan Shock Center Pilot Grant (CJC), NIH R35 122140 (ALS).

Acknowledgements: We thank members of the lab past and present, as well as former and current colleagues and collaborators for their helpful contributions.

Authorship Attributions: IM, CJC, AG, HM, AB, KC, MM, DP, MB, AN, and NN: Performed the experimental work. Reviewed and edited the manuscript. CJC and IM: Wrote and edited the manuscript. CJC and ALS: Conceptualized the experiments outlined here.

ABSTRACT

Skeletal muscle has recently arisen as a novel regulator of Central Nervous System (CNS) function and aging, secreting bioactive molecules known as myokines with proteostasis and metabolism-modifying functions in targeted tissues, including the CNS. Here we report the generation of a novel transgenic mouse with enhanced skeletal muscle proteostasis via targeted overexpression of Transcription Factor E-B, a master regulator of proteostasis and lysosomal function. We have discovered that the resulting enhanced muscle proteostasis function significantly ameliorates proteotoxicity, reduces neuroinflammation and promotes transcriptional remodeling of the aging CNS, preserving cognition and memory in aging mice. Enhancing skeletal muscle proteostasis also reduces neuroinflammation and accumulation of tau-associated pathological hallmarks in a mouse model of tau pathology. Our results implicate the maintenance of skeletal muscle proteostasis throughout aging to direct regulation of the CNS metabolism and function, and suggest that skeletal-muscle originating factors may act as novel therapeutic targets against age-associated neurodegenerative diseases.

INTRODUCTION

Aging is associated with an organism-wide progressive loss of tissue form and function, broadly characterized by the 'hallmarks of aging' [1]. In particular, the aging central nervous system (CNS) [1,2] exhibits a global loss in protein homeostasis (proteostasis), impaired neuroplasticity and resilience, and an increase in neuroinflammation [2,3]. These alterations are believed to render the aging CNS vulnerable to age-associated dysfunction and the development of neurodegenerative disease [2].

Over the last ten years, there has been growing evidence that suggests prominent contributions of the periphery to the etiology of age-associated neurodegenerative diseases [4-8]. In particular, manipulation of skeletal muscle protein quality control pathways yields important benefits to the invertebrate CNS by activating proteostasis and protecting against the accumulation of aggregation-prone neurodegenerative disease proteins in the brain and the retina [5,8,9]. Although the mechanisms responsible for these benefits remain poorly understood, some of these effects are mediated by secreted factors that communicate important metabolic, proteostatic and inflammatory changes between tissues [5,7,9]. Indeed, blood circulating factors have recently arisen as potent regulators of mammalian CNS aging and metabolism [10-13]. For example, exposure to a young plasma environment (either through heterochronic parabiosis or plasma transfers) can rescue function in the aging CNS [12,14] by decreasing neuroinflammation [15] and enhancing neurogenesis [10]. Studies have further demonstrated that increasing the levels of these individual factors in peripheral circulation is sufficient to rejuvenate the aged CNS [12,16,17], supporting the existence of geroprotective circulating factors with CNS targeting effects. Although the source and identity of these neuroprotective circulating cytokines are unclear, several of them are expressed in, and are known to be secreted from, skeletal muscle [5,18-20]. In fact, skeletal muscle acts as an endocrine organ secreting a myriad of bioactive factors that induce metabolic changes in a cell non-autonomous manners in distant tissues like liver [21], adipose tissue [22], and even the CNS [19].

Recently, this muscle-to-brain signaling axis has been proposed to have important implications for CNS aging and age-associated neurodegenerative disease [19,23,24]. Skeletal muscle function has arisen as a key predictor for phenotypic and clinical outcomes in age-associated neurodegenerative diseases, including Alzheimer's Disease (AD) and Parkinson's Disease (PD) [25,26]. Consistent with this, we were the first to uncover a novel mechanistic basis for motor neuron disease in the polyglutamine disease Spinal and Bulbar Muscular Atrophy (SBMA),

where disruption of skeletal muscle autophagy [27] initiates the pathogenic cascade that culminates in neuronal toxicity and death [28,29]. Furthermore, we demonstrated that rescuing proteotoxicity specifically in skeletal muscle was sufficient to rescue motor neuron degeneration and extend lifespan in this model, despite robust misfolded protein burden in the brain [29]. Importantly, we also demonstrated the feasibility and efficacy of peripheral delivery of antisense oligonucleotides targeting skeletal muscle expression of the misfolded protein in rescuing neurological phenotypes [30], confirming that therapeutic reduction of misfolded protein expression in skeletal muscle can have important benefits to the CNS.

A central player in proteostasis is macroautophagy (hereafter referred to as autophagy), which degrades and recycles intracellular material such as mitochondria, protein aggregates, and other large subcellular components too large to be processed through the proteasome. As with most other aging tissues, autophagy activity steadily declines with age in skeletal muscle [31], leading to a chronic accumulation of damaged macromolecules and organelles [31-33] and contributing to the onset of age-associated decline [1,31,34-37]. In accordance with this, genetic disruption of autophagy is sufficient to drive cellular and biochemical hallmarks of aging in young skeletal muscle, including accumulation of protein aggregates [34,36-39], mitochondrial dysfunction [40-43] and compromised metabolic signaling [40,44,45]. Autophagy dysfunction has thus been proposed to act as a primary regulator of biological aging for skeletal muscle [1,31]. Interestingly, well-known interventions that maintain or re-activate global and skeletal muscle autophagy via genetic [46-48], behavioral [49] and pharmacological [50,51] manipulation extend lifespan and/or markers of cognitive health span in murine and primate models. Altogether, this suggests that maintenance of skeletal muscle proteostasis may promote neurotrophic signaling in the brain, providing systemic benefits against disease and age-associated CNS decline.

Skeletal muscle autophagy is regulated in part by Transcription Factor E-B (TFEB), a master regulator of a lysosomal-to-nucleus signaling axis that integrates cellular metabolism and autophagy [52-54]. TFEB expression and function are strongly induced in skeletal muscle in response to interventions with documented neuroprotective effects on the aging [55,56] and neurodegenerative disease-afflicted CNS, including low nutrient conditions [57] and exercise [40]. However, the precise role of TFEB-dependent signaling in skeletal muscle during aging, and its impact on the muscle-to-brain axis remains largely unknown. Here we report the generation of a novel transgenic mouse with enhanced muscle proteostasis via overexpression of TFEB. We have discovered that the resulting enhanced skeletal muscle proteostasis function is maintained throughout the lifespan, protecting against the onset age-associated phenotypes in aging

skeletal muscle. Furthermore, we report that enhancing skeletal muscle proteostasis significantly reduces hippocampal accumulation of neuropathological hallmarks and reduces neuroinflammation in a mouse model of tau pathology, despite no exogenous activation of our transgene in the CNS. Enhancing skeletal muscle proteostasis via TFEB overexpression across the lifespan also ameliorates proteotoxicity, reduces neuroinflammation and promotes transcriptional remodeling of the aging CNS without neurodegenerative disease burden, preserving cognitive performance in aging mice. Our results implicate, for the first time in mammals, maintenance of skeletal muscle proteostasis to direct regulation of CNS health and function, and suggest that skeletal-muscle originating factors may act as novel therapeutic targets against age-associated neurodegenerative diseases.

RESULTS

TFEB overexpression preserves proteostasis-related and metabolism-associated networks in aging skeletal muscle

To allow for tissue-specific expression of TFEB under controlled conditions, we took advantage of the Cre-loxP system for mammalian gene editing. We derived a novel line of conditional transgenic mice carrying the β-actin promoter in combination with the CMV enhancer (CAGGS) and with a floxed 3x-FLAG-eGFP STOP cassette placed just 5' to a 3x-FLAG-human *TFEB* transgene (i.e. fxSTOP-TFEB transgenic mice) (**Figure 1A**). In the presence of Cre-recombinase, the STOP codon cassette will be excised out, allowing expression of the human TFEB transgene, also known as a Cre-loxP ON system. To drive overexpression of TFEB specifically in skeletal muscle, we crossed male fxSTOP-TFEB mice with female Human Skeletal Actin (HSA)-Cre mice to achieve widespread expression of Cre-recombinase only in cells of the myogenic lineage [58].

The resulting cTFEB;HSACre bigenic mice of both sexes exhibited a strong induction of human *TFEB* expression in skeletal muscle tissue (**Supplemental Figure 1A, left**). This exogenous human *TFEB* expression was still quite prominent at 24 months of age in cTFEB;HSACre transgenic skeletal muscle (**Supplemental Figure 1B, left)** suggesting that overexpression of the transgene remains active even at very old ages. Immunoblotting of quadricep skeletal muscle confirmed robust expression of 3x-FLAG-TFEB protein in cTFEB;HSACre bigenic muscle lysates (**Figure 1B**). As TFEB is a transcriptional factor, we confirmed nuclear

localization of human TFEB in cTFEB;HSA-Cre skeletal muscle myonuclei via immunofluorescence (**Supplemental Figure 1C, in white**).

Next, we confirmed TFEB overexpression exclusively in skeletal muscle of cTFEB;HSACre bigenic mice by multiple approaches. First, we confirmed expression of the biologically inert 3x-FLAG-eGFP cassette upstream of the STOP codon (**Figure 1A**) and no exogenous expression of 3x-FLAG-TFEB in other highly metabolic tissues of non-myogenic lineages in cTFEB;HSACre transgenic mice, including brown adipose tissue (**Supplemental Figure 1D**) and liver (**Supplemental Figure 1E**). Consistent with these findings, we also did not detect expression of exogenous 3x-FLAG-TFEB in hemibrain protein lysates (**Supplemental Figure 1F**). Indeed, at all ages examined, we detected no differences in *TFEB* transcription in hippocampal RNA lysates regardless of their genotype or age (**Supplemental Figure 1A & B, right**). To directly assess the Cre-mediated recombination of an additional transgene reporter, we generated TdTomato Ai9;HSACre mice and confirmed robust tdTomato fluorescence in skeletal muscle of bigenic individuals (**Supplemental Figure 1G**). Importantly, and consistent with our results in our cTFEB;HSACre model, there was no detectable TdTomato fluorescence in the CNS (**Supplemental Figure 1H**), including the hippocampus (**Supplemental Figure 1H, insets**) of TdTomato Ai9;HSACre mice, consistent with the muscle-restricted specificity of this HSA-Cre-loxP-ON approach [59]. Overall, these data confirm previous reports of striated muscle-specific Cre-mediated recombination using the HSA-Cre transgenic driver line [58], and demonstrate expression of exogenous *TFEB* only in skeletal muscle of cTFEB;HSACre bigenic mice. This establishes our newly developed inducible fxSTOP-TFEB mouse as an effective model to generate spatiotemporally controlled transgenic expression of human *TFEB*.

TFEB directly regulates transcription of multiple lysosomal and autophagy-associated genes [52,54], promoting lysosomal function and autophagy activation, as well as mitochondrial biogenesis and lipid metabolism in vivo [40,57] and in vitro [52,54]. We confirmed functional activation of TFEB-dependent transcription in cTFEB:HSA-Cre bigenic muscle, using our previously reported TFEB-responsive muscle gene targets [27] including *Lamp1* (an essential lysosomal structural protein), *Atg5* (a key regulator of autophagy initiation), *Ctsd* (Cathepsin D) and *Ctsb* (Cathepsin B, both lysosomal proteases) (**Figure 1C-F**). Immunoblotting studies confirmed significant increases of TFEB transcriptional targets LAMP1 and CTSD at the protein level in cTFEB;HSACre bigenic muscle (**Figure 1G**).Consistent with previous studies demonstrating TFEB overexpression increases the number and size of LAMP1-positive lysosomes in multiple tissues [52,57,60], we also detected significant increases in the number of LAMP1+ puncta and total

LAMP1+ area in cross-sections of female (and similar trends in male) cTFEB;HSACre skeletal muscle (**Figure 1H**). These findings confirm physiologically significant increases in TFEB-dependent transcription [40] and lysosomal biogenesis [40,54] in skeletal muscle of cTFEB:HSA-Cre mice.

Given the principal role of autophagy function to skeletal muscle health [35,45], and the predicted contributions of age-associated autophagy dysfunction to muscle wasting and sarcopenia during aging [61], we sought to examine the overall changes in the skeletal muscle protein landscape in response to TFEB overexpression throughout aging. We performed proteome profiling of young and aged, control and cTFEB;HSACre male quadricep skeletal muscle. Differential abundance analysis of species revealed around 1000 proteins associated with TFEB overexpression in young (6-month-old) skeletal muscle (**Figure 1I**). Of these, 650 (65%) were significantly overrepresented and 350 (35%) were underrepresented in TFEB-overexpressing muscle compared to their littermate controls. At 18 months of age, a time point where age-associated proteostasis dysfunction is prevalent in murine skeletal muscle [62], the same proteomics approach identified around 400 differentially expressed proteins in TFEB-expressing skeletal muscle (**Figure 1J**). Of these, 250 proteins (83%) were significantly enriched and 50 proteins (17%) were significantly decreased in cTFEB;HSACre bigenic muscle. Importantly, at both ages examined, TFEB remained significantly overexpressed (**Figure 1I-J, boxes**), confirming our previous finding of maintenance of exogenous skeletal muscle TFEB expression across the lifespan of our cTFEB;HSACre model (**Supplemental Figure 1A-B**).

To visualize the key networks of differentially expressed proteins associated with TFEB-overexpression, we performed a functional enrichment analysis on all overexpressed proteins using the STRING protein-protein interaction network [63] (**Figure 1K**). Using TFEB as our 'bait' for functional connectivity nodes, we identified two clear interaction networks: one associated with lysosomal biogenesis and function (**Figure 1K, blue**) and a second one associated with key skeletal muscle proteostasis and metabolic signaling pathways including mTOR, AKT and GSK3β (**Figure 1K, green**). Both of these nodes are key elements of the CLEAR signaling network controlled by TFEB-mediated transcription [53,54], were previously reported to be transcriptionally elevated in skeletal muscle after viral-mediated TFEB overexpression [40], and are central regulators of aging [1].

To further understand the functions of all the upregulated proteins in TFEB-overexpressing skeletal muscle, KEGG enrichment analysis was performed. As expected, central proteostasis

categories were significantly upregulated in TFEB-overexpressing skeletal muscle: including Hypoxia-inducible factor 1 (HIF-1) signaling, proteasome, and autophagy/lysosomal function categories (**Figure 1L, orange**), consistent with our targeted immunoblot studies (**Figure 1G**) and our STRING analysis (**Figure 1K**). Importantly, this enrichment in proteostasis categories and TFEB-regulated nodes of signaling was still present in our aging cohorts (**Figure 1L, top**), suggesting that overexpression of TFEB throughout the lifespan preserves proteostasis function in aging skeletal muscle.

TFEB overexpression has been reported to reactivate declining proteostasis associated with age- or disease-associated impaired lysosomal function [27,60,64]. We wondered if the enrichment in proteostasis pathways observed in aged skeletal muscle with TFEB-overexpression would result in functional outcomes reflective of proteostasis maintenance. Analysis of autophagy marker LC3, which is cleaved and post-translationally modified into its mature form (LC3-II) upon autophagy induction [65], revealed a significant increase in LC3-II:LC3-I ratio in quadricep muscle of 12 month-old cTFEB:HSA-Cre mice (**Figure 1M**). This suggests that in addition to activating lysosomal biology and function, expression of TFEB in skeletal muscle results in functional activation of autophagy in vivo, as reported in other TFEB-overexpression studies in skeletal muscle, liver, and brain [57,60,64].

Interestingly, additional functional categories enriched in our proteomics analysis related to cellular metabolism and mitochondrial function, including thermogenesis, oxidative phosphorylation and pyruvate metabolism (**Figure 1L, gold**). We also detected central fatty acid metabolism pathways, including PPAR signaling and metabolism, and degradation and biosynthesis of fatty acids (**Figure 1L, green**). This is consistent with previously published reports suggesting that exogenous TFEB expression in young skeletal muscle induces the expression of genes involved in mitochondrial biogenesis, fatty acid oxidation, and oxidative phosphorylation [40]. Here we confirm for the first time that these changes in cTFEB;HSACre muscle are maintained throughout aging, particularly those associated with mitochondrial metabolism and fatty acid metabolism (**Figure 1L, top, gold and green**).

KEGG analysis also showed enrichment in cTFEB;HSACre bigenic muscle for classical signaling pathways shown to decline during aging, including members of the Insulin-IGF1-signaling (IIS) and AMPK signaling [1] (**Figure 1L, blue**). Finally, we also detected multiple hits for amino acid metabolism pathways, such as catabolism of branched-chain amino acids (BCAAs), including valine, leucine and isoleucine metabolism (**Figure 1L, purple**). Importantly,

these changes were still evident in our aged cohorts (**Figure 1L, top**), suggesting a potential geroprotective effect of TFEB-associated signaling in aging skeletal muscle. In agreement with this, analysis of skeletal muscle of 12-month-old control mice showed marked accumulation of age-associated histopathological markers, including fiber decompaction, intrafibrillary myonuclei and multilamellar structure accumulation (**Figure 1N, top**). Remarkably, these features were mostly absent in skeletal muscle sections from age- and littermate-matched cTFEB:HSA-Cre mice (**Figure 1N, bottom**). Instead, aging cTFEB;HSACre muscle retained compact fiber organization and perifibrillar myonuclei and did not exhibit any multilammelar structures. Indeed, the appearance of the aging cTFEB;HSACre skeletal muscle was much more consistent with their younger counterparts. In agreement with this, we also detected reduced expression of muscle stress factor *Mstn* (myostatin) [66] (**Figure 1O**) and increased expression of metabolic modulator *Fndc5* [66] in aged cTFEB;HSACre skeletal muscle (**Figure 1P**). Altogether, our results suggest maintenance of functional proteostasis and mitochondrial function via TFEB overexpression throughout aging has multiple benefits in skeletal muscle, targeting established hallmarks of aging.

Enhanced skeletal muscle proteostasis reduces accumulation of hyperphosphorylated tau and microglial activation in a mouse model of tau pathology.

To assess the potential neuroprotective effects of enhancing skeletal muscle proteostasis in the context of age-associated neurodegenerative disease pathologies, we derived cTFEB;HSACre transgenic mice in the MAPT P301S (PS19) background. This is a well-known model of neurofibrillary tangle toxicity, a hallmark of AD and related tauopathies [67], and is characterized by prominent accumulation of hippocampal hyperphosphorylated human mutant MAPT protein and pronounced neuroinflammation, including microgliosis and astrocyte reactivity [67].

We first confirmed muscle-restricted 3x-FLAG-TFEB overexpression in skeletal muscle lysates from MAPT P301S;cTFEB;HSACre mice, as well as the presence of human Tau in hippocampal lysates of both groups via immunoblotting (**Figure 2A**). As previously reported [67], at 9 months of age there is robust accumulation of Ser202/Thr205 hyperphosphorylated tau (residues abnormally phosphorylated in paired helical filaments during AD progression) in the dentate gyrus of the hippocampus of MAPT P301S mice of both sexes [67] (**Figure 2B, middle panel**). Conversely, we noted a significant reduction in the total fluorescence counts of AT8-positive phosphorylated tau in the dentate gyrus of MAPT P301S;cTFEB;HSACre mice (**Figure 2B**, **purple**) compared with MAPT P301S littermate controls (**Figure 2B**, **teal**). More so, this

reduction was particularly evident in the levels of 'intracellular tau' accumulating around hippocampal cell bodies (**Figure 2B, insets**), suggesting reduced accumulation of toxic tau species and aggregates [68] in the hippocampus of MAPT P301S;cTFEB;HSACre mice. We confirmed similar but less striking reductions in Thr231 phospho-tau (another primary site of tau phosphorylation associated with neurotoxic tau accumulation) immunostaining (**Supplemental Figure 2A**), suggesting overall reductions in tau hyperphosphorylation in the hippocampus of MAPT P301S transgenic mice with TFEB overexpression in skeletal muscle.

Astrocytes and microglia are key mediators of neuroinflammation, and undergo key morphological and functional alterations during neurodegenerative disease, including changes in ramification and cellular process complexity [69], reduced immune surveillance activity [70] and increased reactivity phenotypes [71]. We confirmed significant increases in the staining for GFAP-positive structures (a marker of astrocyte reactivity) in the dentate gyrus of 9-month-old MAPT P301S mice of both sexes (**Figure 2C, teal**) compared to their MAPT-negative littermate controls (**Figure 2C, gold**). We also detected significant increases in the volume of IBA1+-positive microglia in the same brain region (**Figure 2C, teal**), consistent with previous reports in the MAPT P301S model indicating high levels of neuroinflammation starting as early as 4 months of age [67,72]. Strikingly, we noted significant reductions in both of these pro-inflammatory glial morphometric parameters in the hippocampus of MAPT P301S;cTFEB;HSACre littermates (**Figure 2C, purple**), suggesting overall reduced hippocampal neuroinflammation during symptomatic disease stages through activation of skeletal muscle proteostasis.

Enhancing skeletal muscle proteostasis promotes neurotrophic signaling and reduces hippocampal neuroinflammation in MAPT P301S transgenic mice.

To gain more precise insights into disease-relevant transcriptional changes in the hippocampus of MAPT P301S mice with enhanced skeletal muscle proteostasis, we used the Nanostring nCounter® Alzheimer's Disease panel. This platform directly assesses the expression of 770 genes curated from human and pre-clinical models of AD and robustly captures disease-relevant signatures and their modifications after pre-clinical interventions [73]. Using this approach, we found a total of 79 differentially expressed genes in MAPT P301S;cTFEB;HSACre hippocampi compared to their littermate MAPT P301S+ controls (**Figure 2D-E**). Interestingly, most differentially regulated genes were downregulated (76 of 79), consistent with their identity as transcriptional drivers of disease [73]. Many of these transcripts are associated with microglial activation (including *Rhoc, Bcar3, and Alcam*), markers of neuronal function (*Gdap1l1),*

phospholipid remodeling (*Ano6*), growth factor signaling (*Vgf*), endothelial cell migration and matrix adhesion (*Rras*) and guanine nucleotide exchange factors (*Dock3*). Interestingly, multiple down-regulated genes were associated with novel variants and loci associated with increased polygenic neurodegenerative disease risk (*Prkd3* [74], *Bcar3* [75], *Nfia* [76], and *Elovl7* [77]) as well as predictors of the rate of cognitive decline in AD (*Hecw1* [78]). Interestingly, expression of *Arhgdib,* recently identified as a potential novel biomarker for tau neurofibrillary tangle accumulation and neuropathological Braak stage in human entorhinal cortex [79], was also significantly reduced, consistent with our reduced hyperphosphorylated tau staining in the hippocampus of MAPT P301S ;cTFEB;HSACre transgenic mice (**Figure 2B**). *Pbxip1,* another significantly downregulated marker, has been found to be associated with phosphorylated-tau and $A\beta_{1-40}$ levels in the human temporal cortex [80]. Additional transcriptional reductions of significance include genes of unknown function but classified as transcriptional identifiers of AD progression *(Ptprn, Cpne2,* and *Eri2)* [73]. Functional annotation of the differentially expressed co-expression/functional clusters revealed significant reductions in the nCounter AD microglial activation module (composed of 63 genes associated with microglial activation during AD progression) (**Figure 2F**) in the hippocampi of 9 month old female (but not male) MAPT P301S;cTFEB;HSACre mice compared with MAPT P301S littermates. This is consistent with increased neuroprotection and reduced neuroinflammation in the hippocampus of MAPT P301S mice with enhanced skeletal muscle proteostasis, as suggested by our glail morphometric analysis (**Figure 2C**). Interestingly, we also detected a sex-bias in the trophic factor functional cluster (composed of genes *Arhgdib, Bcl2, Calm3, Camk4, Gab1, Mapk9, Mapkapk2, Ntrk2, Pik3r1* and *Psen1*), with a significant improvement back to baseline expression in the hippocampus of male (but not female) MAPT P301S;cTFEB;HSACre mice (**Figure 2G**). We confirmed activation of neurotrophic signaling as early as 6 months of age in the hippocampus of male MAPT P301S;cTFEB;HSACre mice by targeted qRT-PCR analysis, which showed corrections of declining expression levels of neurotrophic factors *Bdnf* and *Fndc5* back to control littermate levels (**Figure 2H-I**) [23,81]. Importantly, there was also a significant extension (38%) in the lifespan of male MAPT P301S;cTFEB;HSACre mice (**Supplemental Figure 2D**). While the median survival of male MAPT P301S mice was 352 days (**Supplemental Figure 2D, teal curve**), male MAPT P301S;cTFEB;HSACre mice median survival was 489 days (**Supplemental Figure 2D, purple curve).** Although we did not detect a similar lifespan extension in female MAPT P301S;cTFEB;HSACre mice (**Supplemental Figure 2E**), it is worth noting that in our hands, female MAPT P301S transgenic mice already live significantly longer than their male littermate controls (median survival of 468.5 days), perhaps suggesting they have reached

maximal lifespan in this model. Finally, we did not detect any differences in ataxia progression [82] (**Supplemental Figure 2B**) or weight loss (**Supplemental Figure 2C**) between our groups. Altogether, these provocative results suggest that enhanced skeletal muscle proteostasis modifies the accumulation of pathogenic tau isoforms and reduces neuroinflammation in the hippocampus of MAPT P301S mice in a sex-dependent manner via transcriptional remodeling and activation of neurotrophic signaling. Importantly, this occurs in the absence of detectable exogenous human TFEB expression in the CNS (**Supplemental Figure 1**), suggesting an independent mechanism of muscle-to-brain communication underlying these effects.

Skeletal muscle over-expression of TFEB decreases neuroinflammation markers and lipofuscin accumulation in the healthy aged CNS.

To examine the effect of increased skeletal muscle proteostasis on the healthy aging brain without neurodegenerative disease burden, we assessed the transcriptional and functional status of known inflammatory markers in the CNS of healthy aged (20+ months old) control and cTFEB;HSACre mice, an age when global decreases in proteostasis and increases in pro-inflammatory signaling are detectable in most murine tissues [1,83], including the CNS [1,2]. Total hippocampal mRNA levels of *Ccl2* and *Nfκb*, pro-inflammatory cytokines previously reported to mediate microglial responses to inflammation, were significantly reduced in the hippocampus of aging female (but not male) cTFEB;HSACre bigenic mice (**Figure 3A-B**). Interestingly, the expression of *Il6* (interleukin 6) was significantly elevated in the same groups (**Figure 3C**). We also detected significantly higher levels of expression of *Bdnf* (Brain Derived Neurotrophic Factor) in hippocampal lysates from aged male (but not female) mice (**Figure 3D**), similar to what we observed in our MAPT P301;cTFEB;HSACre model (**Figure 2H**).

Using similar morphometric analysis as before to quantify glial cell shape and morphology, we did not detect any differences in microglia (IBA1+) or astrocyte (GFAP+) number, volume or ramification state in the dentate gyrus of aged cTFEB;HSACre bigenic mice compared to their littermate controls (**Figure 3E-F**). This may suggest that the expression differences observed via transcriptional approaches above may either originate in non-glial cells (neurons or endothelial cells, for example) or not translate into detectable morphological changes at the ages examined. It is important to note that age-associated changes in neuroinflammation in an otherwise healthy brain are not as pronounced as those seen in the context of neurodegenerative disease (such as in the MAPT P301S model, for example). Overall, these results suggest a shift in the cytokine transcriptional landscape of the aging hippocampus with

upregulated skeletal muscle proteostasis towards reduced inflammatory signaling in female mice, consistent with what we observed in our MAPT P301S studies (**Figure 2**).

Accumulation of lipofuscin, a non-degradable intracellular auto-fluorescent polymer, becomes prominent in the aging brain, likely reflecting an age-associated decline in basal CNS autophagy [1]. We examined the clearance capabilities of the aging CNS by indirect immunofluorescence of lipofuscin granules in brain sections of aged (21-24 months old) control and cTFEB;HSACre mice. While we detected striking lipofuscin granule accumulation in several brain regions of aged control mice, including the hippocampus (**Figure 3G, top**), there was a significant decrease in lipofuscin deposition in the dentate gyrus of cTFEB;HSACre females (**Figure 3G, bottom),** with a similar non-significant trend in males. To determine any changes in proteostasis associated signaling in this brain region, we next examined the transcriptional levels of multiple autophagy and lysosomal associated genes. Consistent with previous reports, we confirmed significant age-associated increases in the expression of autophagy lysosomal markers *Atg8/Lc3*, *Lamp1, Sqstm1,* and *Ctsd* in the male hippocampus, which has been proposed to occur as a compensation for age-associated decline in proteostasis function (**Figure 3H-K**). Interestingly, these differences were not as prominent in the aging female hippocampus. Furthermore, some of these transcriptional increases were reduced in the hippocampus of aged male cTFEB;HSACre bigenic mice, suggesting that enhancing skeletal muscle proteostasis prevents the age-associated hippocampal proteostasis dysfunction associated with age. Our data thus indicates a potential sex-bias in activation of neuroprotective signaling in the hippocampus of aging cTFEB:HSACre bigenic mice, with females decreasing neuroinflammation (**Figure 3A-C**) and males increasing neurotrophin expression levels (**Figure 3D**). Altogether, our results suggest that overexpression of TFEB in skeletal muscle throughout the lifespan promotes maintenance of protein quality control regulation in the CNS, ultimately reducing proteostatic burden and neuroinflammation in the aging hippocampus, similar to what we observed in our MAPT P301S studies.

Improved performance in neurocognitive testing of aging cTFEB;HSACre mice.

Given the maintenance of proteostasis, reductions in neuroinflammation markers and increases in *Bdnf* expression observed in the aging cTFEB;HSACre hippocampi, we pursued neurocognitive testing in aged (16-18 months old) control and cTFEB;HSACre mice. First, we evaluated spatial learning and memory using the Barnes maze task, a hippocampal working memory test known to be sensitive to aging in mice. We documented significantly faster escape

times (**Figure 3L**) and a significant decrease in the number of errors per trial (**Figure 3M**) in aged cTFEB;HSACre mice of both sexes in comparison to controls. Indeed, by the last trial, cTFEB;HSACre mice escaped the maze twice as quickly as control mice. In the novel object recognition task – an independent behavioral test of hippocampal recognition memory – we also found that aged cTFEB;HSACre mice of both sexes exhibited a significantly greater number of contacts with the novel object compared to controls during the test phase (**Figure 3N**). Indeed, aged cTFEB;HSACre mice have around a ~15% higher preference for the novel object relative to their age-matched littermate controls (**Figure 3O**). Importantly, we also confirmed no differences in body weight (**Figure 3P**), visual performance, and motor activity (not shown) between aged control and cTFEB;HSACre cohorts. We did detect a significant increase in grip strength in aged male (and a similar trend in female) cTFEB;HSACre bigenic mice (**Figure 3Q**), consistent with our findings suggesting that overexpression of TFEB in skeletal muscle can also improve muscle function during aging (**Figure 1**).

Hence, these results provide exciting evidence for a pronounced improvement in neural function in the aging brain of cTFEB;HSACre mice with enhanced muscle proteostasis.

Enhancing skeletal muscle proteostasis transcriptionally remodels the hippocampus of cTFEB;HSACre bigenic mice throughout the lifespan in a sex-dependent manner.

To determine the molecular basis of the benefits of enhancing skeletal muscle proteostasis on the aging CNS, we performed unbiased transcriptome analysis on hippocampal RNAs isolated from young (6 months old) and aged (22-24 months old) mice (**Figures 4-5**). By this time point, aging control animals have increased neuroinflammation (**Figure 3A-B**), have evident CNS proteostasis dysfunction (**Figure 3G**), and display deficits in cognitive function (**Figure 3L-O**), phenotypes that are significantly improved in cTFEB;HSACre mice.

Bulk RNA-Seq analysis of hippocampal RNA lysates revealed robust changes in gene expression in young cTFEB;HSACre bigenic mice compared to their age- and sex-matched littermate controls (**Figure 4, Figure 5, Supplemental Figure 3, and Supplemental Figure 4**). In young female cTFEB;HSACre hippocampi, we detected 1194 differentially expressed genes, (385 up-regulated and 809 down-regulated) (**Figure 4A**). To identify specific neural signaling functions associated with these differentially expressed genes, we performed GO Enrichment analysis. We found that key categories associated with synaptic function, including ion- and voltage-gated channel activity, transporter complexes, as well as synapse and synaptic

membrane categories, were significantly enriched in the hippocampus of young female cTFEB;HSACre mice (**Figure 4C**). Enrichment analysis of differential gene expression (KEGG) revealed additional critical categories associated with neural function, including oxytocin signaling, cAMP signaling, Hippo signaling and gap junctions (**Figure 4E**). Furthermore, metabolic and functional pathway analysis (Reactome) of differentially expressed genes also identified key categories known to regulate cognitive plasticity, including GPCR ligand binding, voltage gated potassium channels, and transmission across chemical synapses, among others (**Supplemental Figure 3A**).

Consistent with our biochemical and functional findings suggesting increased neuroprotective benefits in aging cTFEB;HSACre mice (**Figure 3**), we found that these transcriptional changes modulating synaptic function pathways are still present (although not as prominent) in the aging hippocampus of aged female cTFEB;HSACre mice (**Figure 4B, Figure 4D, Supplemental Figure 3B, and Supplemental Figure 3D**). Indeed, KEGG functional pathways enriched in our aged female hippocampus included key categories associated with preservation of neuronal activity and cognitive function, including axon guidance, HIF-1 signaling, AMPK signaling and PI3-Akt signaling (**Figure 4F**). We confirmed the age-associated differential expression of a subset of our top-hit genes in a second group of hippocampal RNA lysates using targeted qRT-PCR (**Supplemental Figure 3E**). Altogether, this suggests that overexpression of TFEB in skeletal muscle activates multiple neuroprotective gene networks associated with synaptic function and signaling in the female hippocampus, and that this transcriptional remodeling is preserved through aging.

Analysis of the functional enrichment of top differentially expressed genes in the hippocampus of young male cTFEB;HSACre mice revealed a different pattern. We detected 1797 differentially expressed genes (928 up-regulated and 869 down-regulated), which GO-term analysis associated mostly with multiple mitochondria or ribosomal/transcription targeting pathways (**Figure 5A and C**). This included mitochondrial respiratory chain, mitochondrial protein complexes, electron transport chain and ATP metabolic processes (**Figure 5C**). Additional enriched metabolic pathways in the hippocampus of young cTFEB;HSACre males included non-sense mediated decay, metabolism of RNA and translation (**Supplemental Figure 4A**). Consistent with this, KEGG analysis revealed the most enriched functional pathways were ribosomes and oxidative phosphorylation (**Figure 5E**). As before, we confirmed the differential expression of a random sampling of our top-hit genes using targeted qRT-PCR (**Supplemental Figure 4E).** When we performed similar analysis on the male aging hippocampus, we only

detected 539 differentially expressed genes in the hippocampus of aged male cTFEB;HSACre mice (279 up-regulated, 261 down-regulated) (**Figure 5B**), with only mild significance on functional pathways (**Figure 5D, Figure 5F, Supplemental Figure 4B, and Supplemental Figure 4D**). Our results thus strongly suggest a sex bias in the hippocampal transcriptional responses associated with muscle-TFEB overexpression, with the female hippocampi up-regulating neuronal signaling and synaptic function and the male hippocampi upregulating transcriptional and mitochondrial responses. Finally, many of these changes are preserved up until late stages in the lifespan of our model (24 months of age), suggesting that these transcriptional changes may underlie the neurocognitive benefits observed in our aging cTFEB;HSACre cohorts.

DISCUSSION

Skeletal muscle comprises roughly 40% of the total body mass in a healthy young adult human and is highly susceptible to age-associated proteostatic decline [32,33]. Skeletal muscle autophagy facilitates metabolic reprogramming and mitochondrial quality control during conditions of high metabolic demand [34,57,84] and is also required to maintain muscle health and muscle mass [35,85,86]. Skeletal muscle health has been linked to multiple chronic age-associated conditions, including diabetes [87], cardiovascular disease [88] and, more recently, neurodegenerative diseases [24-26]. Here, and for the first time in mammals, we provide direct evidence demonstrating the benefits of enhanced skeletal muscle proteostasis on the brain throughout aging and in the context of neurodegenerative proteinopathy. We find that life-long overexpression of TFEB (a master regulator of proteostasis and metabolism) reduces the development of age-associated biochemical hallmarks in skeletal muscle. Indeed, we detected robust up-regulation of multiple fundamental aging pathways [89], including proteostasis and mitochondrial function (**Figure 1**). We also detected important changes in branched-chain amino acid signaling, which have been recently linked to lifespan and healthspan extension in rodents [90], indicating that maintenance of proteostasis through TFEB overexpression has pan-geroprotective effects on aging skeletal muscle.

The hippocampus is a critical structure in cognitive aging, and hippocampal atrophy and dysfunction are key features of both aging and neurodegenerative diseases [91,92]. In addition to rescuing age-associated hallmarks in skeletal muscle, we also discovered significant improvements in multiple disease-associated biochemical hallmarks in the aging hippocampus of cTFEB;HSACre transgenic mice, ultimately preserving cognitive function in the aging brain.

Importantly, we observed these benefits without any detectable expression of our transgene in the CNS (**Supplemental Figure 1**), suggesting that the observed reductions in proteotoxicity and neuroinflammation (**Figure 2**), as well as the improved neurocognitive performance of aged cTFEB;HSACre mice (**Figure 3**) are due solely to the overexpression of TFEB in the skeletal muscle.

Tauopathies are clinically, biochemically and morphologically heterogeneous neurodegenerative diseases characterized by the deposition of abnormal aggregates of tau in the brain. The MAPT P301S model recapitulates multiple aspects of tauopathies, including microglial activation, filamentous tau inclusions and synapse loss [67]. Our studies indicate that enhancing skeletal muscle proteostasis has significant benefits on multiple markers of gliosis in this model of tau toxicity, reducing astrocytic GFAP expression and the volume of microglia present in the hippocampus of MAPT P301S mice (**Figure 2C**). This suggests that enhancing muscle proteostasis in MAPT P301S mice reduces microglial and astrocyte activation in the hippocampus, ultimately reducing neuroinflammation. Indeed, we confirmed significantly reduced transcriptional activation of the nCounter AD microglial activation panel (**Figure 2F**), a proxy for pro-inflammatory signaling in the context of AD-associated pathologies [81]. This highlights both the robust pro-inflammatory state associated with tau pathogenesis, as well as the intriguing possibility that manipulation of skeletal muscle proteostasis pathways may represent a novel target for modulation of inflammation in the CNS.

Previous transcriptional studies of the healthy aging hippocampus have identified dysregulation of ion homeostasis, disruption of neurotransmission, and ribosome biogenesis as key biological process exhibiting differential regulation with aging [2,93]. Specifically, genes related to synaptic transmission and plasticity appear to be particularly sensitive to age-associated transcriptional dysregulation (reviewed here [3]). Many of these gene networks are also significantly altered in AD and other associated tauopathies [81]. Importantly, similar networks were transcriptionally remodeled in the healthy aging cTFEB;HSACre hippocampus, underscoring potential new mechanisms of neuroprotective benefits. Further studies to identify specific responders in the CNS (during healthy aging or in the context of neurodegenerative disease) may yield fascinating new insights into avenues for therapeutic development.

Manipulation of skeletal muscle proteostasis modulates expression of similar functional enrichment categories (ie. Trophic factor signaling, neuroinflammation) in the aging and tau-afflicted hippocampus of our cTFEB;HSACre mice in a sex-dependent manner. Interestingly, we

detected significant reductions in the accumulation of hyperphosphorylated tau in both sexes in the MAPT P301S model, suggesting differential mechanisms may underlie the neuroprotective benefits mediated by enhancing skeletal muscle proteostasis. While it is unclear whether these differential responses between male and female hippocampi to the enhancement of skeletal muscle proteostasis reflect local differences in the CNS itself or peripheral differences in the expression, secretion or trafficking of circulating signals, they underscore the fundamental need to examine sex differences contributing to the biology of aging and neurodegenerative diseases.

Recent evidence has shown that muscle-originating circulating factors (myokines) appear to play central roles in regulating CNS health and function. For example, Amyrel amylase, a skeletal muscle secreted protein with maltose producing function, was identified as a key proteostasis stress-induced myokine with CNS targeting effects in *Drosophila Melanogaster* [5]. Consistent with our own findings here, muscle-specific *amyrel* overexpression improves proteostasis and prevents neurodegeneration induced by aggregation-prone disease-associated pathogenic proteins in the fly brain and retina [5]. Another example is Fibronectin-domain III containing 5 (FNDC5), a glycosylated type 1 membrane protein that is highly enriched in skeletal muscle. FNDC5 can be proteolytically cleaved into an N-terminal fragment known as irisin, which is then released into circulation [87]. Recent studies have demonstrated that peripheral delivery of irisin reduces neuroinflammation and rescues cognitive decline in two separate mouse models of AD, and is a central modulator of cognitive function [19]. Likewise, the lysosomal protease CTSB is secreted from skeletal muscle into circulation in response to exercise and is required for the full manifestation of exercise-associated benefits on the CNS, including increases in the levels of hippocampal BDNF and the activation of neurogenesis [20]. Interestingly, recent evidence demonstrates pronounced involvement of the macroautophagic/autophagic molecular machinery in cellular secretion [94]. Indeed, key signaling molecules and cytokines associated with inflammation, such as IL1B (interleukin 1 beta) and IL6 (interleukin 6), are released into the extracellular space via autophagy-dependent secretion [94]. There is also a growing body of evidence that age [66] and exercise [95], known modifiers of skeletal muscle proteostasis and metabolism, alter the composition of the totality of factors produced and secreted by skeletal muscle. This suggests that activation of muscle proteostasis via TFEB-overexpression may, in addition to the local geroprotective benefits in muscle tissue, also be modifying the skeletal muscle ‘secretome’, potentially enriching it with neurotrophic factors or depleting it from neurotoxic factors, although this hypothesis remains to be tested.

Importantly, our work indicates for the first time that one potential mechanism underlying the neuroprotective benefits associated with enhancing skeletal muscle proteostasis is a reduction in neuroinflammation, particularly in the female hippocampus. Although previous work examining the muscle-to-brain axis has demonstrated important benefits on the accumulation of misfolded protein inclusions in the CNS [5,8,19] (similar to what we observed in the MAPT P301S;cTFEB;HSACre hippocampus), the profound reductions in both morphological and transcriptional markers of neuroinflammation observed in this model suggest modulation of skeletal muscle proteostasis may be a novel target to modulate neuroinflammatory signaling in vivo in the context of aging and/or neurodegenerative diseases.

Over the last ten years, there has been growing evidence that suggests prominent contributions of the periphery to the etiology of neurodegenerative diseases. Our discovery that skeletal muscle proteostasis can be a crucial site for regulation of CNS health and function provides compelling evidence for a new therapeutic delivery avenue into the brain, providing a currently unexplored new diagnostic and therapeutic intervention site (i.e. skeletal muscle) for preserving brain health.

METHODS

Generation of fxSTOP-TFEB transgenic mice.

We used a pCMV-human TFEB expressing vector from Origene (clone # sc122773), used previously [27]. We cloned a 3x-FLAG fragment via insertion into the Acc65I and Pac1 restriction sites of the targeting vector. The fxSTOP-TFEB vector was generated in multiple steps, as follows: (1) 5′ and 3′ targeting arms were inserted by PCR onto the ends of a minimal 1.8 kb, chloramphenicol-resistant vector; (2) an ampicillin resistance cassette was cloned into the MluI, XmaI sites of the targeting vector; (3) an 1.1 kb fragment encoding the actin promoter, a loxP site, a 3x-FLAG tag fused to EGFP was cloned into the NheI, PacI restriction sites of the targeting vector; (4) a 2.8 kb fragment containing the second loxP site, followed by 3x-FLAG-human TFEB sequence. The final fxSTOP-FLAG-human TFEB vector was microinjected into C57BL/6J:C3H/HeJ F1 hybrid oocytes. Of six founders identified, two gave rise to fxSTOP-FLAG-human TFEB lines with comparable phenotypes. Of these lines, we chose to focus our studies principally on line 419. The presence of the floxed 3x-FLAG-eGFP STOP-3x-FLAG-human TFEB cassette is verified by allele dependent qPCR genotyping analysis with each generation (Transnetyx), and expression of the 3x-FLAG-eGFP sequence (upstream of the STOP codon) in single transgenic fxSTOP-TFEB mice is assessed every other generation. We confirmed excision of 3x-FLAG-EGFP-STOP cassette in the presence of Cre-recombinase by crossing fxSTOP-TFEB transgenic female mice with HSA-Cre transgenic mice (JAX Strain No: 006139 | HSA-Cre79), and corresponds to the HSA-Cre driver mouse line from the laboratory of Dr. Judith Melki. TdTomato mice (B6.Cg-Gt(ROSA)26Sor$^{tm9(CAG\text{-}tdTomato)Hze/J}$, JAX Strain #:007909) express robust tdTomato fluorescence following Cre-mediated recombination, is congenic on the C57BL/6J genetic background and were also obtained from JAX. The MAPT P301S line (Stock No: 008169) originated in the laboratory of Dr. Virginia Lee. cTFEB;HSACre;MAPT P301S transgenic mice were generated by crossing fxSTOP-TFEB females to MAPT P301S males. Female double transgenic offspring was then crossed with heterozygote HSA-Cre transgenic males. All commercially available lines were obtained directly from JAX. All lines have been maintained in a C57/B6 background for over ten generations in our lab. Mice were housed in a temperature- and humidity-controlled environment on a 12-hour light/dark cycle with food and water ad libitum. Mice of both sexes were used for all experiments in equal numbers, or as close to equal numbers as possible. For all MAPT P301 experiments, control animals are MAPT P301S-;fxSTOP-TFEB-;HSACre- and/or MAPT P301S-;fxSTOP-TFEB+;HSACre- littermates. For all aging experiments, control animals are fxSTOP-TFEB-

;HSACre- and/or fxSTOP-TFEB+;HSACre- littermates. In our hands, we did not detect any differences on tau or aging-associated CNS phenotypes on fxSTOP-TFEB+ animals compared to the wild-type controls. All animal experimentation adhered to NIH guidelines and was approved by and performed in accordance with the University of California, San Diego, Duke University and University of Alabama at Birmingham Institutional Animal Care and Use. The fxSTOp-TFEB line of transgenic mice is available for sharing with academic institutions free-of-charge. For-profit institutions will adhere to UCSD's policy regarding copyrighted material.

Tissue Collections

Animals were anesthetized with 3.8% Avertin Solution. All animals received a transcardial perfusion with 60 mLs of cold 1x PBS. Half of CNS tissue (right/left hemi-brain) was post-fixed in 4% PFA for less than 24 hours before being transferred to 30% sucrose for another 24 hours before cryo-sectioning and staining the other half was micro-dissected into cortex and hippocampus and flash-frozen in liquid nitrogen for RNA and protein analyses. Half of skeletal muscle tissue (right/left limb muscle) was fresh frozen in OCT following dissection, while the other half was flash-frozen in liquid nitrogen for RNA and protein analyses.

RT-PCR Analysis

Flash frozen perfused isolated mouse tissues (quadriceps, hippocampus) were placed in plastic tubes with silica beads (MP Biomedical, 116913100) and homogenized in TRIzol (Invitrogen, 15596026). RNA was extracted via standard phenol-chloroform procedures followed by DNase digestion (Thermo Fisher, AM2238). cDNA was generated using iScript (Bio-Rad Technologies, 1708891). Quantitative PCR was run using Sybrgreen (Life Technologies, 4309155) for chemical detection (Applied Biosystems; QuantStudio 3). Enrichment was determined based on double-delta CT value. Primers were ordered from IDT Predesigned qPCR Assays unless otherwise specified. Primers used are listed in Primer Table 1.

ImmunoBlot Analysis

Protein lysates from muscle tissue was prepared as previously described [27,29]. Protein concentration was quantified using a Pierce™ BCA Protein Assay (23227). Fifty or 25 µg of homogenized proteins were loaded per lane, and after running Any KD, 10%, or 4-15% Mini-PROTEAN TGX Gels (BioRad, 4568124, 4561034, and 4561084), samples were transferred to 0.2 µm (for LC3) or 0.45 µm (for everything else) PVDF membranes (BioRad, 162-0175 and

1704275), which were blocked in 5% BSA in PBS at RT for 1 hr. Membranes were incubated with anti-FLAG antibody (Sigma, M2, 1:1000), anti-TFEB antibody (Cell Signaling, 4240,1:1000), anti-Lamp1 antibody (Novus Bio, NB600-956, 1:1000), anti-LC3 antibody (Cell Signaling, 2775S, 1:1000) or anti-GAPDH (Invitrogen, AM4300, 1:5000) in PBS-T with 5% BSA at 4°C overnight. The primary antibody was visualized with horseradish-peroxidase conjugated anti-rabbit at (Cell Signaling, 7074P2, 1:5,000) and enhanced chemiluminescence (BioRad, 170-5060) or goat-anti-mouse IgG 680 (Invitrogen, A21058, 1:10,000). Densitometry analysis was performed using the BioRad Image Lab 6.1 software application.

Immunoflourescence Studies

Tissue was embedded in OCT (TissueTek, 4583), frozen utilizing 2-methylbutane (VWR, 103525-278) submerged in liquid nitrogen and stored at -80C until used. All samples were sectioned on a standing cryostat (Leica). Sections of brain were 20 microns, while muscle tissue was 15 microns thick. For immunohistochemistry, sections were permeabilized with .25% Triton for 15 mins and blocked with 4% BSA for 30 minutes-1 hour. Brain sections were then incubated with anti-GFAP (ab4674, Abcam, 1:200), anti-IBA1 (Wako, 019-19741, 1:200), anti-AT180 TAU (Thermo, MN1040, 1:100) and anti-AT8 TAU (Invitrogen, MN1020, 1:100) while muscle sections were incubated with anti-laminin (Sigma, L9393, 1:200), anti-FLAG (Sigma, F1804, 1:1000), anti-LC3 (Cell Signaling, 2775S, 1:200), anti-LAMP1 (DHSB, 1D4B, 1:100) and anti-hTFFEB (CST, 4240, 1:200) overnight at 4°C and incubated with secondary antibodies at RT for 1 hour (both diluted in 4% BSA). Next the slides were washed with Hoescht (Thermo Scientific, 62249, 1:5000) and mounted with prolong glass (Invitrogen, P36984). All slides were washed with 1X PBS three times for 5 minutes each between steps.

Slides were imaged in the UAB HIRF HRIF Confocal/Light Microscopy Core utilizing the 10x objective on the Nikon A15R/SIM Confocal microscope. Z-stacks of the entire hippocampus area/section were collected, and max intensity projections were generated using FIJI. Lipofuscin imaging was performed using an epifluorescent Nikon light microscope with a 20x objective. For TdTomato imaging, stitched whole-section z-stacks were acquired using a Nikon A1R HD25 confocal microscope of nuclei in the blue channel and native TdTomato fluorescence in the red channel.

For quantification of astrocyte and/or microglia parameters, raw ND2 files were uploaded to the NIS elements platform and thresholds were set to eliminate background in each channel in

order to delineate each object. Morphometric information was collected in addition to the automated counting of objects. A size exclusion parameter was used for GFAP positive objects under 10 microns, IBA-1 positive objects under 15 microns, and any object larger than 5,000 microns were all excluded due to standard assessments of cell sizes. FIJI was used for quantification of lipofuscin and LAMP1 puncta.

Quantitative proteomics sample preparation and data-independent acquisition mass spectrometry.

We identified distinct protein species from crude total extractions of whole quadricep muscle by mass spectrometry after trypsin digestion, in collaboration with the University of Washington Nathan Shock Center Protein Phenotypes of Aging Proteomics Core. Quadricep muscle powder samples were processed and digested using S-Trap Micro Spin Column (Protifi, C02-micro-80) following the manufacturer's protocol. SDS (5%) lysis and solubilization buffer were added to liver powder samples and homogenized on ice using a sonicator probe. Protein concentrations were determined using Pierce BCA Protein Assay Kit (Thermo Fisher Scientific, PI23227). Proteins were digested at 1 ug trypsin to 25 ug protein ratio on S-Trap at 47°C for 1 h. Peptides extracted from S-Trap were dried with a vacuum concentrator and reconstituted in 0.1% formic acid in water prior to mass spectrometry acquisition. Data were acquired using data-independent acquisition (DIA) on a Thermo EASY-nLC 1000 and a Thermo Q-Exactive HF orbitrap mass spectrometer. Peptides were separated using PicoFrit Self-Packed Columns (360 µm OD x 75 µm ID; New Objective, Woburn, MA) packed to 30 cm with 3 µm ReproSil-Pur C18 beads (ESI Source Solutions, r13.aq.0001). The trap column was packed to 2 cm with same C18 beads using 360 µm OD x 150 µm ID fused silica capillary fritted with Kasil on one end. Solvent A was 0.1% formic acid in water, and solvent B was 0.1% formic acid in 80% acetonitrile. For each injection, 1 µg of sample was loaded and eluted using a 90-min gradient from 5% to 45% B at 250 nL/min. DIA methods followed the chromatogram library workflow as described in detail previously [96]. All muscle samples were pooled in equal ratio to create a muscle library sample. The library samples were used to generate chromatogram libraries using the strategy described before [97]. Thermo Q Exactive HF MS was used to acquire six gas phase fractionated runs spanning a total mass range of 400 to 1000 m/z, each with staggered 4 m/z narrow precursor isolation windows [98]. EncyclopeDIA software suite was used to generate a chromatogram library [96] and retention time models for all peptides detected at 1% FDR determined by Percolator [99]. For quantitative DIA run, equal amounts of protein were used for each sample. A 24 × 24 m/z staggered window from 400.43190 to 1000.7048 m/z was used as

described previously [98]. EncyclopeDIA software suite was used to search the chromatogram library with calibrated retention time and quantify peptides and proteins in each sample.

Proteomics Analysis

A linear model was fit to the protein level data using the Bioconductor limma package [100], and the estimated SVs were adjusted as covariates in our model. The limma package uses empirical Bayes moderated statistics, which improves power by 'borrowing strength' between proteins in order to moderate the residual variance [101]. Adjusted P value was calculated with Benjamini-Hochberg method across groups (young transgenic, young control, old transgenic, and old control). Proteins were sorted for significant differential expression using a cutoff of less than 5% FDR and greater than 1.5 foldchange in young and old cohorts as a change due to skeletal muscle overexpression of humanized TFEB. Volcano plots were created in R studio with ggplot and ggrepel. Significantly upregulated proteins in cTFEB;HSA-Cre mice were queried using the KEGG pathway analyzer, which is a feature of STRING's web tool [63]. Bar graphs were created in Rstudio with the ggplot2 packages.

Significantly upregulated proteins, up to two degrees from TFEB, were entered into STRINGdb web tool for functional network analysis. A confidence interaction score of 0.70 and MCL clustering was applied to the networks. The networks were exported from STRING and imported into Cytoscape for further style editing [102].

Gene Expression Analysis.

RNA Sequencing and Bioinformatics Analysis

RNA was extracted as mentioned above from flash frozen hippocampal tissue for four biological replicates (sex/genotype) and checked for quality. mRNA libraries were prepared by Novogene (Novogene Corporation INC, Sacramento, CA, United States) and bulk RNA-seq analysis was performed via NovaSeq PE150 (Illumina, San Diego, CA, United States) high throughput sequencing. Bioinformatics analysis for differentially expressed genes was performed by Novogene.

Nanostring nCounter AD panel

Assays were performed with 100 ng aliquots of RNA using the NanoString nCounter Analysis system (NanoString Technologies, Seattle, WA, USA) at the UAB Nanostring Core, following previously described and established protocols [73]. Counts for target genes were normalized to house-keeping genes included in the panel (*Cltc, Gapdh, Gusb, Hprt, Pgk1,* and *Tubb5*). After codeset hybridization overnight, the samples were washed and immobilized to a cartridge using the NanoString nCounter Prep Station. Cartridges were scanned in the nCounter Digital Analyzer at 555 fields of view for the maximum level of sensitivity. Gene expression was normalized using NanoStringNorm R package. Specifically, background correction was performed using the negative control at the cutoff of mean + 2 standard deviation. All p values were adjusted using a false discovery rate (FDR) correction of 1% for multiple comparisons. Housekeeping genes were used to for normalization based on geometric mean. Data and heat analyses were performed in the nSolver Analysis Software 2.0. Gene expression values were presented as the percentage of the MAPT P301S group for comparison of MAPT P301S pathogenesis to the MAPT P301S;cTFEB;HSACre cohort.

Mouse Phenotyping and Behavioral Studies.

Barnes Maze

The Barnes maze apparatus is an opaque Plexiglas disc 75 cm in diameter elevated 58 cm above the floor by a tripod. Twenty holes, 5 cm in diameter, are located 5 cm from the perimeter, and a black Plexiglas escape box (19 x 8 x 7 cm) is placed under one of the holes. Distinct spatial cues are located all around the maze and are kept constant throughout the study. On the first day of testing, a training session was performed, which consists of placing the mouse in the escape box for one minute. After the one-minute habituation period, the first session was started. At the beginning of each session, the mouse was placed in the middle of the maze in a 10 cm high cylindrical black start chamber. After 10 seconds the start chamber was removed, a buzzer (80 dB) and a light (400 lux) were turned on, and the mouse was set free to explore the maze. The session ended when the mouse entered the escape tunnel or after 3 min elapsed. When the mouse entered the escape tunnel, the buzzer was turned off and the mouse was allowed to remain in the dark for one minute. When the mouse did not enter the tunnel by itself it was gently put in the escape box for one minute. The tunnel was always located underneath the same hole (stable within the spatial environment), which was randomly determined for each mouse. Mice were tested once a day for 4 days for the acquisition portion of the study. For the 5th test (probe test), the escape tunnel was removed and the mouse was

allowed to freely explore the maze for 3 min. The time spent in each quadrant was determined and the percent time spent in the target quadrant (the one originally containing the escape box) was compared with the average percent time in the other three quadrants. This was a direct test of spatial memory as there was no potential for local cues to be used in the mouse's behavioral decision. Two weeks later the mice were tested again with the escape box in the original position (retention test). This allows for the examination of long term memory. Finally, on the day after this test, the escape tunnel was moved to a new location (90 degrees from the original position) and the behavior of the mouse was recorded. This is called the reversal test and it allows for the examination of perseveration at the old hole as well as the working memory strategies the mice adopted to locate the new tunnel location. Each session was videotaped and scored by an experimenter blind to the genotype of the mouse. Measures recorded include the latency to enter the escape box and the number of errors made per session. Errors are defined as nose pokes and head deflections over any hole that did not have the tunnel beneath it. The probe data were analyzed using Noldus Ethovision software to determine time spent in each quadrant of the maze as well as to assess activity measures.

Novel Object Recognition

Mice were individually habituated to a 51cm x 51cm x 39cm open field for 5 min. Mice were then tested with two identical objects placed in the field (either two 250 ml amber bottles or two clear plastic cylinders 6x6x16cm half filled with glass marbles). An individual animal was allowed to explore for 5 min, now with the objects present. After two such trials (each separated by 1 minute in a holding cage), the mouse was tested in the object novelty recognition test in which a novel object replaced one of the familiar objects (for example, an amber bottle if the cylinders were initially used). All objects and the arena were thoroughly cleaned with 70% ethanol between trials to remove odors. Behavior was video recorded and then scored for number contacts (touching with nose or nose pointing at object and within 0.5 cm of object) and/or for time contacting the objects. Habituation to the objects across the familiarization trials (decreased contacts) was an initial measure of learning and then renewed interest (increased contacts) in the new object indicated successful object memory. Recognition indexes were calculated using the following formula: (# contacts during test)/(# contacts in last familiarization trial + # contacts during test). Values greater than 0.5 indicate increased interest, whereas values less than 0.5 indicate decreased interest in the object during the test relative to the final familiarization trial.

Statistical Analysis

All data were analyzed by t-test, 1-way, 2-way or 3-way between-subject ANOVA with post hoc comparisons depending on the number of variables and groups in each analysis. For ANOVA, if statistical significance ($p < 0.05$) was achieved, we performed post hoc analysis to account for multiple comparisons. The level of significance (α) was always set at 0.05. Survival curves were analyzed using Log-rank (Mantel-Cox) Test. Data were analyzed using Prism 7 (GraphPad Software, La Jolla, CA) and are represented as means and standard error of the means. All experiments and data analyses were conducted in a blinded fashion. All data were prepared for analysis with standard spread sheet software (Microsoft Excel).

Figure Legends

Figure 1: Autophagy and lysosomal activation in skeletal muscle protects against age-associated phenotypes.

(A) Schematic depicting 3x-FLAG human TFEB transgene. Cassettes are arranged from 5' (left) to 3' (right). Note that the 3x-FLAG-EGFP-STOP cassette (flanked by loxP sites) prevents expression of the 3x-FLAG human TFEB transgene unless in the presence of Cre recombinase β-actin promoter.

(B) Immunoblot of control (left) and cTFEB;HSACre (right) quadriceps lysates. Transgenic 3x-FLAG-TFEB protein weighs ~50 kDa (arrow). Non-specific band is shown below as a loading control (asterisk).

(C-F) qRT-PCR for *Lamp1* (C), *Atg5* (D), *Ctsd* (E), and *CtsB* (F) expression in quadriceps mRNA lysates from young (6 months old) male cTFEB;HSACre mice and controls.

(G) Immunoblot analysis for LAMP1 and Cathepsin D protein in quadriceps protein lysates from young (6 months old) female cTFEB;HSACre mice and controls. Densitometry quantification relative to average of control individuals shown below.

(H) Representative images of gastrocnemius from young (6-7 months old) control and cTFEB;HSACre mice stained for LAMP1 (green), nuclei/Hoescht (blue). Quantification of LAMP1+ puncta and LAMP1+ area/muscle section are shown on the right. Each data point represents the average of 10 separate images collected from 3-5 sections/individual. Scale bars = 100 μm.

(I-J) Volcano plot of proteomics analysis depicting differentially regulated proteins in young (I, 6 months old, I) and aged (J, 18 months old) cTFEB;HSACre quadriceps muscle relative to controls. Overexpressed proteins in red, underexpressed proteins in blue. Note that TFEB itself (rectangles) is highly expressed in both aged and young muscle.

(K) STRING predicted protein-protein interactions of overexpressed proteins from (I) showing predicted interacting networks converging on TFEB (blue) and mTOR (green).

(L) KEGG enrichment analysis clusters overexpressed proteins from (I-J) into categories associated with proteostasis and autophagy (orange), mitochondrial metabolism (gold), fatty acid metabolism (green), age-associated signaling (blue), and amino acid metabolism (purple).

(M) Immunoblot for LC3 protein levels in quadriceps lysates from young (6 months old) female cTFEB;HSACre and controls. Densitometry quantification of LC3II/LC3I Ratio (normalized to tubulin) shown below.

(N) Representative images of tibialis anterior cross sections stained for Hematoxylin/Eosin (left) and Trichrome (right) in aged (16 months old) control and cTFEB;HSACre transgenic mice. Intrafibrillary myonuclei (yellow, arrows) and multilaminar structures (yellow, asterisks) are indicated. Scale bars = 20 µm.

(O-P) qRT-PCR for *Mstn* (O) and *Fndc5* (P) expression in quadriceps mRNA lysates from aged (20-22 months old) cTFEB;HSACre and controls.

Each point represents the average of all sections from an individual. Controls are age-matched littermates. Unless otherwise stated, data are presented as mean ± SEM * $p<0.05$, ** $p<0.01$, T-test.

Figure 2: Skeletal muscle TFEB-overexpression reduces accumulation of hyperphosphorylated tau and microglial activation in a mouse model of tau pathology.

(A) Immunoblot of 3x-FLAG TFEB protein in quadriceps muscle lysates from 9-month old MAPT P301S;cTFEB;HSACre and MAPT P301S mice (top). Immunoblot for total Tau protein (T6 antibody) in hippocampal lysates from same individuals (bottom). GAPDH is shown below as a loading control.

(B) Representative merged images of the hippocampus dentate gyrus stained for phosphorylated tau (AT8, white) and nuclei/Hoescht (blue) in 9-month old control (top, in gold), MAPT P301S (middle, in teal), and MAPT P301S;cTFEB;HSACre mice (bottom, in purple). Insets depicting perinuclear AT8 staining are 5X zooms of areas demarcated by yellow squares. Quantification of total phosphotau staining/section (right, top) and for intracellular phosphotau staining, (right, bottom). Each point represents the average of all sections containing the dentate gyrus (2-3 sections) for an individual animal. Scale bars = 100 µm.

(C) Representative merged images of the dentate gyrus stained for astrocytes (GFAP, green), microglia (IBA1, red) and nuclei (Hoescht, blue) in 9-month old control (top, gold), MAPT P301S (middle, teal), and MAPT P301S;cTFEB;HSACre mice (bottom, purple). Insets depicting glia morphology are 5X zooms of areas demarcated by yellow squares. Quantification of IBA1+ microglia volume (top, right) and GFAP+ astrocyte staining amounts per section (bottom, right). Each point represents the average of all sections containing the dentate gyrus (2-3 sections) for an individual animal. Scale bars = 100 µm.

(D-E) Volcano plot of differentially expressed genes in the hippocampi of 9-month old male (D) and female (E) MAPT P301S;cTFEB:HSACre animals relative to age-matched P301S MAPT littermates using the Nanostring nCounter AD panel. Down-regulated genes in blue, up-regulated genes in red.

(F-G) Nanostring nCounter AD panel cluster analysis of differentially expressed genes from D-E for gene clusters associated with microglial activation (F) and with trophic factors (G) in MAPT P301S;cTFEB;HSACre hippocampi (purple) compared to P301S MAPT (teal) age-matched littermates. Analysis done via nSolver (Nanostring) differential gene expression analysis software. Each point represents a single individual hippocampal mRNA lysate.
(H-I) qRT-PCR for *Bdnf* (H) and *Fndc5* (I) expression in hippocampal RNA lysates from 9-month old male MAPT P301S (teal) and MAPT P301S;cTFEB;HSACre mice (purple) relative to controls (not shown).
Controls are littermates. Unless otherwise noted, data are represented as mean ± SEM * $p<0.05$, ** $p<0.01$,*** $p<0.001$, One-way ANOVA, post-hoc T-test (B,C) and t-test (F-I).

Figure 3: Skeletal muscle TFEB-overexpression decreases neuroinflammation, lipofuscin accumulation, and improves cognitive performance in aged mice.
(A-D) qRT-PCR for *Ccl2* (A), *Nfkb* (B), *Il6* (C), and *Bdnf* (D) expression in hippocampal mRNA lysates from 18-month old cTFEB;HSACre mice and controls.
(E-F) Representative images dentate gyrus of the hippocampus stained for Hoescht (blue), IBA1 (E, red), and GFAP (F, green) in 18-22-month old control (top) and cTFEB;HSACre (bottom) mice. Insets depicting glia morphology are 5X zooms of areas demarcated by yellow squares. Quantification of IBA1+ microglial volume (E, top right) and IBA1+ branching index (E, bottom right). Average number of GFAP+ astrocytes pixels per section (F, top) and GFAP+ astrocyte branching index (F, bottom). Each point represents the average of all sections containing the dentate gyrus from an individual mouse. Scale bars = 100 µm.
(G) Representative merged images of the dentate gyrus of 18-22-month old control (top) and cTFEB;HSACre (middle) mice stained for Hoescht (blue), and lipofuscin puncta (autofluorescence, green). Insets depicting autofluorescent puncta within the dentate gyrus are 5X zooms of areas demarcated by yellow squares. Scale bars = 100 µm.
(H-K) qRT-PCR for *Atg8/LC3* (H), *Lamp1* (I), *Sqstm1* (J), and *Ctsd* (K) expression in hippocampal lysates from young (6 months old, closed diamonds) and aged (21 months old, open diamonds) cTFEB;HSACre mice (purple diamonds) and controls (gold diamonds).
(L-Q) Neurocognitive phenotyping of aged (18 months old) cTFEB;HSACre and control animals. Barnes maze (L,M), novel object recognition (N,O) total body weight (P) and grip strength (Q). Controls are age-matched littermates. Data are represented as mean ± SEM * $p<0.05$, ** $p<0.01$, One-way ANOVA or two-way RMANOVA, post-hoc T-test.

Figure 4: Transcriptome changes in the hippocampi of female cTFEB;HSACre transgenic mice suggest synaptic remodeling and improved synaptic function.

(A-B) Volcano plot of differentially expressed genes in hippocampal lysates from female young (A, 6 months old) and aged (B, 24 months old) cTFEB;HSACre mice relative to controls.

(C-D) GO term analysis of differentially expressed genes from A and B including gene counts and adjusted p values. Boxes highlight neurotrophic signaling pathways.

(E-F) KEGG analysis of differentially expressed genes from A and B. Number of differentially expressed genes (DE) are shown above each category. Arrows highlight categories associated with neural function.

Figure 5: Transcriptome changes in the hippocampi of male cTFEB;HSACre transgenic mice suggest activation of mitochondrial and ribosomal signaling.

(A-B) Volcano plot of differentially expressed genes in hippocampal lysates from male young (A, 6 months old) and aged (B, 24 months old) cTFEB;HSACre mice relative to controls.

(C-D) GO term analysis of differentially expressed genes from A and B including gene counts and adjusted p values. Boxes highlight ribosomal and mitochondrial pathways.

(E-F) KEGG analysis of differentially expressed genes from A and B. Number of differentially expressed genes (DE) are shown above each category. Arrows highlight ribosomal and mitochondrial pathways.

Supplemental Figures

Supplemental Figure 1

(A-B) qRT-PCR analysis for human *TFEB* mRNA expression in 6-month old (A) and 21-month old (B) cTFEB;HSACre quadriceps skeletal muscle (left) and hippocampus (right) compared to controls.

(C) Representative images of gastrocnemius cross sections stained for Hoescht (blue) and Human TFEB (white). Insets of nuclear hTFEB staining are 5x zooms of the areas denoted by the yellow squares. Scale bars = 100 µm.

(D-F) Immunoblot analysis for 3x-FLAG TFEB protein expression from lysates of brown adipose (D), liver (E), and brain (F) tissue from 6-month old cTFEB;HSACre mice and age-matched control littermates. cTFEB;HSACre skeletal muscle lysates are shown in the first lane of each

blot as a positive control for 3x-FLAG TFEB expression. FLAG-eGFP protein cassette (arrow) as well as non-specific bands (asterisks) are indicated.

(G) Representative images of quadriceps and gastrocnemius cross sections from 7-week old TdTomato;HSACre transgenic mice stained for Hoescht (blue), TdTomato (red), and Laminin (white). Scale bars = 100 µm.

(H) Representative images of hemibrain sections from TdTomato;HSACre transgenic mice stained for Hoescht (blue), TdTomato (red). Insets of hippocampal regions are 5x zooms of the areas denoted by the yellow squares. Scale bars = 1 cm.

Controls are age-matched littermates. Data are represented as mean ± SEM, T-test, * $p<0.05$, ** $p<0.01$, *** $p<0.001$.

Supplemental Figure 2

(A) Representative images of the hippocampal dentate gyrus from 9-month old control (top), MAPT P301S (middle), and MAPT P301S;cTFEB;HSACre (bottom) mice stained for Hoescht (blue) and AT180 PhosphoTau (white). Insets of hippocampal regions are 5x zooms of the areas denoted by the yellow squares. Scale bars= 100 µm.

(B) Cumulative ataxia score of 9-month old control, MAPT P301S, and MAPT P301S;cTFEB;HSACre mice.

(C) Weight (in grams) of 11-month old control MAPT P301S, and MAPT P301S;cTFEB;HSACre mice.

(D-E) Survival curves for male (D) and female (E) control, MAPT P301S, and MAPT P301S;cTFEB;HSACre mice.

Controls are age-matched littermates. Data are represented as mean ± SEM, One-way ANOVA post-hoc T-test or Log-rank (Mantel-Cox) test * $p<0.05$, ** $p<0.01$.

Supplemental Figure 3

(A-B) Reactome analysis of differentially expressed genes in hippocampal mRNA lysates from female young (6 months old, A) and aged (24 months old, B) cTFEB;HSACre mice. Number of differentially expressed genes (DE) are shown above each category.

(C-D) GO enrichment analysis of differentially expressed genes from A-B. Number of differentially expressed genes (DE) are shown above each category.

(E) qRT-PCR analysis for select DE genes in hippocampal mRNA lysates from female young (6 months old, solid circles) and aged (24 months old, open circles) control (gold) and cTFEB;HSACre (purple) mice. Expression levels normalized to young controls.

Controls are age-matched littermates. Data are represented as mean ± SEM, One-way ANOVA post-hoc T-test * $p<0.05$, ** $p<0.01$.

Supplemental Figure 4

(A-B) Reactome analysis of differentially expressed genes in hippocampal mRNA lysates from male young (6 months old, A) and aged (24 months old, B) cTFEB;HSACremice. Number of differentially expressed genes (DE) are shown above each category.

(C-D) GO enrichment analysis of differentially expressed genes from A-B. Number of differentially expressed genes (DE) are shown above each category.

(E) qRT-PCR analysis for select DE genes in hippocampal mRNA lysates from female young (6 months old, solid circles) and aged (24 months old, open circles) control (gold) and cTFEB;HSACre (purple) mice. Expression levels normalized to young controls. Controls are age-matched littermates. Data are represented as mean ± SEM, One-way ANOVA post-hoc T-test * $p<0.05$, ** $p<0.01$.

REFERENCES

1 Lopez-Otin, C., Blasco, M. A., Partridge, L., Serrano, M. & Kroemer, G. The hallmarks of aging. *Cell* **153**, 1194-1217, doi:10.1016/j.cell.2013.05.039 (2013).

2 Mattson, M. P. & Arumugam, T. V. Hallmarks of Brain Aging: Adaptive and Pathological Modification by Metabolic States. *Cell Metab* **27**, 1176-1199, doi:10.1016/j.cmet.2018.05.011 (2018).

3 Ham, S. & Lee, S. V. Advances in transcriptome analysis of human brain aging. *Exp Mol Med* **52**, 1787-1797, doi:10.1038/s12276-020-00522-6 (2020).

4 Demontis, F., Patel, V. K., Swindell, W. R. & Perrimon, N. Intertissue control of the nucleolus via a myokine-dependent longevity pathway. *Cell Rep* **7**, 1481-1494, doi:10.1016/j.celrep.2014.05.001 (2014).

5 Rai, M. *et al.* Proteasome stress in skeletal muscle mounts a long-range protective response that delays retinal and brain aging. *Cell Metab* **33**, 1137-1154 e1139, doi:10.1016/j.cmet.2021.03.005 (2021).

6 Durieux, J., Wolff, S. & Dillin, A. The cell-non-autonomous nature of electron transport chain-mediated longevity. *Cell* **144**, 79-91, doi:10.1016/j.cell.2010.12.016 (2011).

7 Taylor, R. C. & Dillin, A. XBP-1 is a cell-nonautonomous regulator of stress resistance and longevity. *Cell* **153**, 1435-1447, doi:10.1016/j.cell.2013.05.042 (2013).

8 Demontis, F. & Perrimon, N. FOXO/4E-BP signaling in Drosophila muscles regulates organism-wide proteostasis during aging. *Cell* **143**, 813-825, doi:10.1016/j.cell.2010.10.007S0092-8674(10)01143-8 [pii] (2010).

9 van Oosten-Hawle, P., Porter, R. S. & Morimoto, R. I. Regulation of organismal proteostasis by transcellular chaperone signaling. *Cell* **153**, 1366-1378, doi:10.1016/j.cell.2013.05.015 (2013).

10 Villeda, S. A. *et al.* The ageing systemic milieu negatively regulates neurogenesis and cognitive function. *Nature* **477**, 90-94, doi:10.1038/nature10357 (2011).

11 Conboy, I. M. *et al.* Rejuvenation of aged progenitor cells by exposure to a young systemic environment. *Nature* **433**, 760-764, doi:10.1038/nature03260 (2005).

12 Castellano, J. M. *et al.* Human umbilical cord plasma proteins revitalize hippocampal function in aged mice. *Nature* **544**, 488-492, doi:10.1038/nature22067 (2017).

13 Schaum, N. *et al.* Ageing hallmarks exhibit organ-specific temporal signatures. *Nature* **583**, 596-602, doi:10.1038/s41586-020-2499-y (2020).

1017 14 Villeda, S. A. *et al.* Young blood reverses age-related impairments in cognitive function and
1018 synaptic plasticity in mice. *Nat Med* **20**, 659-663, doi:10.1038/nm.3569 (2014).
1019 15 De Miguel, Z. *et al.* Exercise plasma boosts memory and dampens brain inflammation via
1020 clusterin. *Nature*, doi:10.1038/s41586-021-04183-x (2021).
1021 16 Horowitz, A. M. *et al.* Blood factors transfer beneficial effects of exercise on neurogenesis and
1022 cognition to the aged brain. *Science* **369**, 167-173, doi:10.1126/science.aaw2622 (2020).
1023 17 Ozek, C., Krolewski, R. C., Buchanan, S. M. & Rubin, L. L. Growth Differentiation Factor 11
1024 treatment leads to neuronal and vascular improvements in the hippocampus of aged mice. *Sci*
1025 *Rep* **8**, 17293, doi:10.1038/s41598-018-35716-6 (2018).
1026 18 Wrann, C. D. *et al.* Exercise induces hippocampal BDNF through a PGC-1α/FNDC5 pathway. *Cell*
1027 *Metab* **18**, 649-659, doi:10.1016/j.cmet.2013.09.008 (2013).
1028 19 Islam, M. R. *et al.* Exercise hormone irisin is a critical regulator of cognitive function. *Nat Metab*
1029 **3**, 1058-1070, doi:10.1038/s42255-021-00438-z (2021).
1030 20 Moon, H. Y. *et al.* Running-Induced Systemic Cathepsin B Secretion Is Associated with Memory
1031 Function. *Cell Metab* **24**, 332-340, doi:10.1016/j.cmet.2016.05.025 (2016).
1032 21 White, P. J. *et al.* Protectin DX alleviates insulin resistance by activating a myokine-liver
1033 glucoregulatory axis. *Nat Med* **20**, 664-669, doi:10.1038/nm.3549 (2014).
1034 22 Quinn, L. S., Anderson, B. G., Strait-Bodey, L., Stroud, A. M. & Argilés, J. M. Oversecretion of
1035 interleukin-15 from skeletal muscle reduces adiposity. *American Journal of Physiology-*
1036 *Endocrinology and Metabolism* **296**, E191-E202 (2009).
1037 23 Lourenco, M. V. *et al.* Exercise-linked FNDC5/irisin rescues synaptic plasticity and memory
1038 defects in Alzheimer's models. *Nat Med* **25**, 165-175, doi:10.1038/s41591-018-0275-4 (2019).
1039 24 Gupta, R., Khan, R. & Cortes, C. J. Forgot to Exercise? Exercise Derived Circulating Myokines in
1040 Alzheimer's Disease: A Perspective. *Front Neurol* **12**, 649452, doi:10.3389/fneur.2021.649452
1041 (2021).
1042 25 Boyle, P. A., Buchman, A. S., Wilson, R. S., Leurgans, S. E. & Bennett, D. A. Association of muscle
1043 strength with the risk of Alzheimer disease and the rate of cognitive decline in community-
1044 dwelling older persons. *Arch Neurol* **66**, 1339-1344, doi:10.1001/archneurol.2009.240 (2009).
1045 26 Kim, J. *et al.* Association of muscle and visceral adipose tissues with the probability of
1046 Alzheimer's disease in healthy subjects. *Sci Rep* **9**, 949, doi:10.1038/s41598-018-37244-9 (2019).
1047 27 Cortes, C. J. *et al.* Polyglutamine-expanded androgen receptor interferes with TFEB to elicit
1048 autophagy defects in SBMA. *Nature neuroscience* **17**, 1180-1189, doi:10.1038/nn.3787 (2014).

1049 28 Cortes, C. J. & La Spada, A. R. Motor neuron degeneration in spinal and Bulbar Muscular Atrophy
1050 is a skeletal muscle-driven process: Relevance to therapy development and implications for
1051 related motor neuron diseases. *Rare Dis* **2**, e962402, doi:10.4161/2167549X.2014.962402
1052 (2014).
1053 29 Cortes, C. J. *et al.* Muscle expression of mutant androgen receptor accounts for systemic and
1054 motor neuron disease phenotypes in spinal and bulbar muscular atrophy. *Neuron* **82**, 295-307,
1055 doi:10.1016/j.neuron.2014.03.001 (2014).
1056 30 Lieberman, A. P. *et al.* Peripheral androgen receptor gene suppression rescues disease in mouse
1057 models of spinal and bulbar muscular atrophy. *Cell Rep* **7**, 774-784,
1058 doi:10.1016/j.celrep.2014.02.008 (2014).
1059 31 Aman, Y. *et al.* Autophagy in healthy aging and disease. *Nat Aging* **1**, 634-650,
1060 doi:10.1038/s43587-021-00098-4 (2021).
1061 32 Jiao, J. & Demontis, F. Skeletal muscle autophagy and its role in sarcopenia and organismal
1062 aging. *Curr Opin Pharmacol* **34**, 1-6, doi:10.1016/j.coph.2017.03.009 (2017).
1063 33 Wohlgemuth, S. E., Seo, A. Y., Marzetti, E., Lees, H. A. & Leeuwenburgh, C. Skeletal muscle
1064 autophagy and apoptosis during aging: effects of calorie restriction and life-long exercise. *Exp*
1065 *Gerontol* **45**, 138-148, doi:10.1016/j.exger.2009.11.002 (2010).
1066 34 Grumati, P. *et al.* Autophagy is defective in collagen VI muscular dystrophies, and its reactivation
1067 rescues myofiber degeneration. *Nat Med* **16**, 1313-1320, doi:10.1038/nm.2247 (2010).
1068 35 Masiero, E. *et al.* Autophagy is required to maintain muscle mass. *Cell Metab* **10**, 507-515,
1069 doi:10.1016/j.cmet.2009.10.008 (2009).
1070 36 Masiero, E. & Sandri, M. Autophagy inhibition induces atrophy and myopathy in adult skeletal
1071 muscles. *Autophagy* **6**, 307-309 (2010).
1072 37 Nascimbeni, A. C., Fanin, M., Masiero, E., Angelini, C. & Sandri, M. The role of autophagy in the
1073 pathogenesis of glycogen storage disease type II (GSDII). *Cell death and differentiation* **19**, 1698-
1074 1708, doi:10.1038/cdd.2012.52 (2012).
1075 38 Hara, T. *et al.* Suppression of basal autophagy in neural cells causes neurodegenerative disease
1076 in mice. *Nature* **441**, 885-889, doi:nature04724 [pii]10.1038/nature04724 (2006).
1077 39 Komatsu, M. *et al.* Loss of autophagy in the central nervous system causes neurodegeneration in
1078 mice. *Nature* **441**, 880-884, doi:nature04723 [pii]10.1038/nature04723 (2006).

1079 40 Mansueto, G. *et al.* Transcription Factor EB Controls Metabolic Flexibility during Exercise. *Cell*
1080 *Metab* **25**, 182-196, doi:10.1016/j.cmet.2016.11.003 (2017).
1081 41 Mammucari, C. *et al.* FoxO3 controls autophagy in skeletal muscle in vivo. *Cell Metab* **6**, 458-
1082 471, doi:10.1016/j.cmet.2007.11.001 (2007).
1083 42 Romanello, V. & Sandri, M. Mitochondrial Quality Control and Muscle Mass Maintenance. *Front*
1084 *Physiol* **6**, 422, doi:10.3389/fphys.2015.00422 (2015).
1085 43 Sandri, M. *et al.* PGC-1alpha protects skeletal muscle from atrophy by suppressing FoxO3 action
1086 and atrophy-specific gene transcription. *Proc Natl Acad Sci U S A* **103**, 16260-16265,
1087 doi:10.1073/pnas.0607795103 (2006).
1088 44 Kim, K. H. *et al.* Autophagy deficiency leads to protection from obesity and insulin resistance by
1089 inducing Fgf21 as a mitokine. *Nat Med* **19**, 83-92, doi:10.1038/nm.3014 (2013).
1090 45 Kustermann, M. *et al.* Loss of the novel Vcp (valosin containing protein) interactor Washc4
1091 interferes with autophagy-mediated proteostasis in striated muscle and leads to myopathy in
1092 vivo. *Autophagy* **14**, 1911-1927, doi:10.1080/15548627.2018.1491491 (2018).
1093 46 Lapierre, L. R. *et al.* The TFEB orthologue HLH-30 regulates autophagy and modulates longevity
1094 in Caenorhabditis elegans. *Nature communications* **4**, 2267, doi:10.1038/ncomms3267 (2013).
1095 47 Pyo, J. O. *et al.* Overexpression of Atg5 in mice activates autophagy and extends lifespan. *Nature*
1096 *communications* **4**, 2300, doi:10.1038/ncomms3300 (2013).
1097 48 Simonsen, A. *et al.* Promoting basal levels of autophagy in the nervous system enhances
1098 longevity and oxidant resistance in adult Drosophila. *Autophagy* **4**, 176-184, doi:5269 [pii]
1099 (2008).
1100 49 Colman, R. J. *et al.* Caloric restriction delays disease onset and mortality in rhesus monkeys.
1101 *Science* **325**, 201-204, doi:10.1126/science.1173635325/5937/201 [pii] (2009).
1102 50 Eisenberg, T. *et al.* Induction of autophagy by spermidine promotes longevity. *Nat Cell Biol* **11**,
1103 1305-1314, doi:10.1038/ncb1975ncb1975 [pii] (2009).
1104 51 Harrison, D. E. *et al.* Rapamycin fed late in life extends lifespan in genetically heterogeneous
1105 mice. *Nature* **460**, 392-395, doi:10.1038/nature08221nature08221 [pii] (2009).
1106 52 Settembre, C. *et al.* TFEB links autophagy to lysosomal biogenesis. *Science* **332**, 1429-1433,
1107 doi:10.1126/science.1204592 (2011).

1108 53 Palmieri, M. *et al.* Characterization of the CLEAR network reveals an integrated control of
1109 cellular clearance pathways. *Human molecular genetics* **20**, 3852-3866, doi:ddr306
1110 [pii]10.1093/hmg/ddr306 (2011).

1111 54 Sardiello, M. *et al.* A gene network regulating lysosomal biogenesis and function. *Science* **325**,
1112 473-477, doi:1174447 [pii]10.1126/science.1174447 (2009).

1113 55 Morgan, T. E. *et al.* The mosaic of brain glial hyperactivity during normal ageing and its
1114 attenuation by food restriction. *Neuroscience* **89**, 687-699, doi:10.1016/s0306-4522(98)00334-0
1115 (1999).

1116 56 van Praag, H., Shubert, T., Zhao, C. & Gage, F. H. Exercise enhances learning and hippocampal
1117 neurogenesis in aged mice. *The Journal of neuroscience : the official journal of the Society for*
1118 *Neuroscience* **25**, 8680-8685, doi:10.1523/jneurosci.1731-05.2005 (2005).

1119 57 Settembre, C. *et al.* TFEB controls cellular lipid metabolism through a starvation-induced
1120 autoregulatory loop. *Nature cell biology* **15**, 647-658, doi:10.1038/ncb2718 (2013).

1121 58 Leu, M. *et al.* Erbb2 regulates neuromuscular synapse formation and is essential for muscle
1122 spindle development. *Development* **130**, 2291-2301 (2003).

1123 59 Madisen, L. *et al.* A robust and high-throughput Cre reporting and characterization system for
1124 the whole mouse brain. *Nat Neurosci* **13**, 133-140, doi:10.1038/nn.2467 (2010).

1125 60 Spampanato, C. *et al.* Transcription factor EB (TFEB) is a new therapeutic target for Pompe
1126 disease. *EMBO Mol Med* **5**, 691-706, doi:10.1002/emmm.201202176 (2013).

1127 61 Lee, D. E., Bareja, A., Bartlett, D. B. & White, J. P. Autophagy as a Therapeutic Target to Enhance
1128 Aged Muscle Regeneration. *Cells* **8**, doi:10.3390/cells8020183 (2019).

1129 62 Giacomello, E. *et al.* Age Dependent Modification of the Metabolic Profile of the Tibialis Anterior
1130 Muscle Fibers in C57BL/6J Mice. *Int J Mol Sci* **21**, doi:10.3390/ijms21113923 (2020).

1131 63 Szklarczyk, D. *et al.* The STRING database in 2021: customizable protein-protein networks, and
1132 functional characterization of user-uploaded gene/measurement sets. *Nucleic Acids Res* **49**,
1133 D605-D612, doi:10.1093/nar/gkaa1074 (2021).

1134 64 Decressac, M. *et al.* TFEB-mediated autophagy rescues midbrain dopamine neurons from alpha-
1135 synuclein toxicity. *Proc Natl Acad Sci U S A* **110**, E1817-1826, doi:10.1073/pnas.1305623110
1136 (2013).

1137 65 Klionsky, D. J. *et al.* Guidelines for the use and interpretation of assays for monitoring autophagy
1138 (3rd edition). *Autophagy* **12**, 1-222, doi:10.1080/15548627.2015.1100356 (2016).

1139 66 Mancinelli, R. *et al.* Biological Aspects of Selected Myokines in Skeletal Muscle: Focus on Aging.
1140 *Int J Mol Sci* **22**, doi:10.3390/ijms22168520 (2021).
1141 67 Yoshiyama, Y. *et al.* Synapse loss and microglial activation precede tangles in a P301S tauopathy
1142 mouse model. *Neuron* **53**, 337-351, doi:10.1016/j.neuron.2007.01.010 (2007).
1143 68 Moloney, C. M., Lowe, V. J. & Murray, M. E. Visualization of neurofibrillary tangle maturity in
1144 Alzheimer's disease: A clinicopathologic perspective for biomarker research. *Alzheimers Dement*
1145 **17**, 1554-1574, doi:10.1002/alz.12321 (2021).
1146 69 Jurga, A. M., Paleczna, M. & Kuter, K. Z. Overview of General and Discriminating Markers of
1147 Differential Microglia Phenotypes. *Front Cell Neurosci* **14**, 198, doi:10.3389/fncel.2020.00198
1148 (2020).
1149 70 Rozovsky, I., Finch, C. E. & Morgan, T. E. Age-related activation of microglia and astrocytes: in
1150 vitro studies show persistent phenotypes of aging, increased proliferation, and resistance to
1151 down-regulation. *Neurobiol Aging* **19**, 97-103, doi:10.1016/s0197-4580(97)00169-3 (1998).
1152 71 Godbout, J. P. *et al.* Exaggerated neuroinflammation and sickness behavior in aged mice
1153 following activation of the peripheral innate immune system. *FASEB J* **19**, 1329-1331,
1154 doi:10.1096/fj.05-3776fje (2005).
1155 72 Sidoryk-Wegrzynowicz, M. *et al.* Astrocytes in mouse models of tauopathies acquire early
1156 deficits and lose neurosupportive functions. *Acta Neuropathol Commun* **5**, 89,
1157 doi:10.1186/s40478-017-0478-9 (2017).
1158 73 Preuss, C. *et al.* A novel systems biology approach to evaluate mouse models of late-onset
1159 Alzheimer's disease. *Mol Neurodegener* **15**, 67, doi:10.1186/s13024-020-00412-5 (2020).
1160 74 de Rojas, I. *et al.* Common variants in Alzheimer's disease and risk stratification by polygenic risk
1161 scores. *Nature communications* **12**, 3417, doi:10.1038/s41467-021-22491-8 (2021).
1162 75 Scelsi, M. A. *et al.* Genetic study of multimodal imaging Alzheimer's disease progression score
1163 implicates novel loci. *Brain* **141**, 2167-2180, doi:10.1093/brain/awy141 (2018).
1164 76 Kim, B. H., Nho, K., Lee, J. M. & Alzheimer's Disease Neuroimaging, I. Genome-wide association
1165 study identifies susceptibility loci of brain atrophy to NFIA and ST18 in Alzheimer's disease.
1166 *Neurobiol Aging* **102**, 200 e201-200 e211, doi:10.1016/j.neurobiolaging.2021.01.021 (2021).
1167 77 Li, G. *et al.* Association of GALC, ZNF184, IL1R2 and ELOVL7 With Parkinson's Disease in Southern
1168 Chinese. *Front Aging Neurosci* **10**, 402, doi:10.3389/fnagi.2018.00402 (2018).
1169 78 Sherva, R. *et al.* Genome-wide association study of the rate of cognitive decline in Alzheimer's
1170 disease. *Alzheimers Dement* **10**, 45-52, doi:10.1016/j.jalz.2013.01.008 (2014).

1171 79 Chai K, L. J., Zhang X, Gu H, Cao P, Ye W, Tang H, Liu J, Chen S, Wan F, Liu GL, Shen D. ARHGDIB
1172 Plays a Novel Role in the Braak Stages of Alzheimer's Diseases via the Immune Response
1173 Mediated by Microglia *Pre-print: Research Square*, doi:10.21203/rs.3.rs-474315/v1 (2021).

1174 80 Simon, M. J. *et al.* Transcriptional network analysis of human astrocytic endfoot genes reveals
1175 region-specific associations with dementia status and tau pathology. *Sci Rep* **8**, 12389,
1176 doi:10.1038/s41598-018-30779-x (2018).
1177 81 Knopman, D. S. *et al.* Alzheimer disease. *Nat Rev Dis Primers* **7**, 33, doi:10.1038/s41572-021-
1178 00269-y (2021).
1179 82 Guyenet, S. J. *et al.* A simple composite phenotype scoring system for evaluating mouse models
1180 of cerebellar ataxia. *J Vis Exp*, doi:10.3791/17871787 [pii] (2010).

1181 83 Lehallier, B. *et al.* Undulating changes in human plasma proteome profiles across the lifespan.
1182 *Nat Med* **25**, 1843-1850, doi:10.1038/s41591-019-0673-2 (2019).
1183 84 He, C., Sumpter, R., Jr. & Levine, B. Exercise induces autophagy in peripheral tissues and in the
1184 brain. *Autophagy* **8**, 1548-1551, doi:10.4161/auto.21327 (2012).
1185 85 Raben, N. *et al.* Suppression of autophagy in skeletal muscle uncovers the accumulation of
1186 ubiquitinated proteins and their potential role in muscle damage in Pompe disease. *Human*
1187 *molecular genetics* **17**, 3897-3908, doi:10.1093/hmg/ddn292 (2008).
1188 86 Vainshtein, A., Grumati, P., Sandri, M. & Bonaldo, P. Skeletal muscle, autophagy, and physical
1189 activity: the menage a trois of metabolic regulation in health and disease. *J Mol Med (Berl)* **92**,
1190 127-137, doi:10.1007/s00109-013-1096-z (2014).
1191 87 Bostrom, P. *et al.* A PGC1-alpha-dependent myokine that drives brown-fat-like development of
1192 white fat and thermogenesis. *Nature* **481**, 463-468, doi:10.1038/nature10777 (2012).
1193 88 Otaka, N. *et al.* Myonectin Is an Exercise-Induced Myokine That Protects the Heart From
1194 Ischemia-Reperfusion Injury. *Circ Res* **123**, 1326-1338, doi:10.1161/CIRCRESAHA.118.313777
1195 (2018).
1196 89 Lopez-Otin, C., Blasco, M. A., Partridge, L., Serrano, M. & Kroemer, G. Hallmarks of aging: An
1197 expanding universe. *Cell* **186**, 243-278, doi:10.1016/j.cell.2022.11.001 (2023).
1198 90 Yu, D. *et al.* The adverse metabolic effects of branched-chain amino acids are mediated by
1199 isoleucine and valine. *Cell Metab* **33**, 905-922 e906, doi:10.1016/j.cmet.2021.03.025 (2021).

1200 91 Adler, D. H. *et al.* Characterizing the human hippocampus in aging and Alzheimer's disease using
1201 a computational atlas derived from ex vivo MRI and histology. *Proc Natl Acad Sci U S A* **115**,
1202 4252-4257, doi:10.1073/pnas.1801093115 (2018).
1203 92 Ivanisevic, J. *et al.* Metabolic drift in the aging brain. *Aging (Albany NY)* **8**, 1000-1020,
1204 doi:10.18632/aging.100961 (2016).
1205 93 Ximerakis, M. *et al.* Single-cell transcriptomic profiling of the aging mouse brain. *Nat Neurosci*
1206 **22**, 1696-1708, doi:10.1038/s41593-019-0491-3 (2019).
1207 94 New, J. & Thomas, S. M. Autophagy-dependent secretion: mechanism, factors secreted, and
1208 disease implications. *Autophagy* **15**, 1682-1693, doi:10.1080/15548627.2019.1596479 (2019).
1209 95 Chow, L. S. *et al.* Exerkines in health, resilience and disease. *Nat Rev Endocrinol* **18**, 273-289,
1210 doi:10.1038/s41574-022-00641-2 (2022).
1211 96 Searle, B. C. *et al.* Chromatogram libraries improve peptide detection and quantification by data
1212 independent acquisition mass spectrometry. *Nature communications* **9**, 5128,
1213 doi:10.1038/s41467-018-07454-w (2018).
1214 97 Pino, L. K., Just, S. C., MacCoss, M. J. & Searle, B. C. Acquiring and Analyzing Data Independent
1215 Acquisition Proteomics Experiments without Spectrum Libraries. *Mol Cell Proteomics* **19**, 1088-
1216 1103, doi:10.1074/mcp.P119.001913 (2020).
1217 98 Amodei, D. *et al.* Improving Precursor Selectivity in Data-Independent Acquisition Using
1218 Overlapping Windows. *J Am Soc Mass Spectrom* **30**, 669-684, doi:10.1007/s13361-018-2122-8
1219 (2019).
1220 99 Kall, L., Canterbury, J. D., Weston, J., Noble, W. S. & MacCoss, M. J. Semi-supervised learning for
1221 peptide identification from shotgun proteomics datasets. *Nat Methods* **4**, 923-925,
1222 doi:10.1038/nmeth1113 (2007).
1223 100 Ritchie, M. E. *et al.* limma powers differential expression analyses for RNA-sequencing and
1224 microarray studies. *Nucleic Acids Res* **43**, e47, doi:10.1093/nar/gkv007 (2015).
1225 101 Smyth, G. K. Linear models and empirical bayes methods for assessing differential expression in
1226 microarray experiments. *Stat Appl Genet Mol Biol* **3**, Article3, doi:10.2202/1544-6115.1027
1227 (2004).
1228 102 Shannon, P. *et al.* Cytoscape: a software environment for integrated models of biomolecular
1229 interaction networks. *Genome Res* **13**, 2498-2504, doi:10.1101/gr.1239303 (2003).

1230

Figure 1

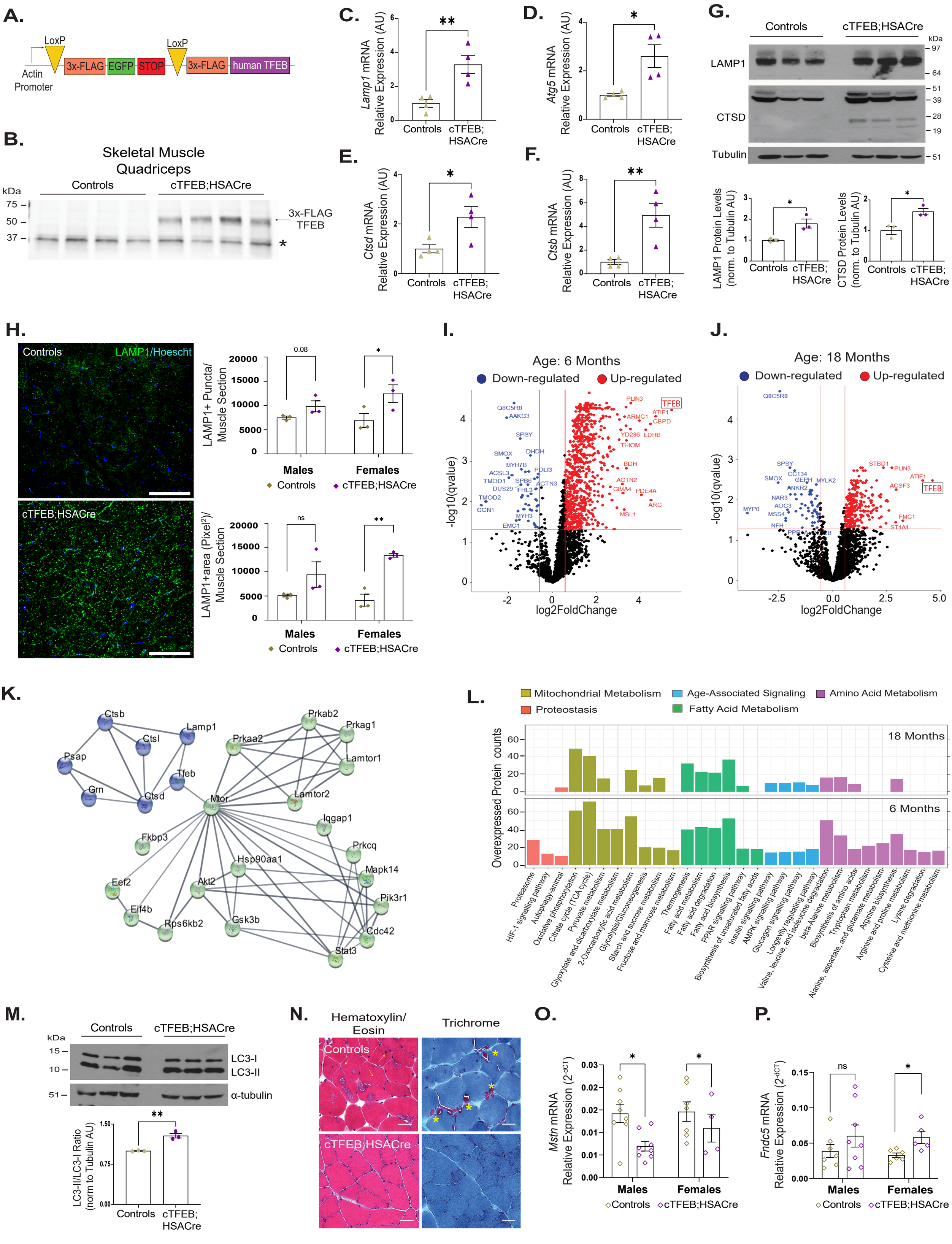
A.
LoxP
LoxP
Actin Promoter
3x-FLAG
EGFP
STOP
3x-FLAG
human TFEB
B.
Skeletal Muscle Quadriceps
Controls
cTFEB;HSACre
kDa
75
50
37
3x-FLAG TFEB
*
C.
Lamp1 mRNA Relative Expression (AU)
**
Controls
cTFEB; HSACre
D.
Atg5 mRNA Relative Expression (AU)
*
E.
Ctsd mRNA Relative Expression (AU)
*
F.
Ctsb mRNA Relative Expression (AU)
**
G.
Controls
cTFEB;HSACre
kDa
LAMP1
CTSD
Tubulin
97
64
51
39
28
19
51
LAMP1 Protein Levels (norm. to Tubulin AU)
CTSD Protein Levels (norm. to Tubulin AU)
H.
Controls
LAMP1/Hoescht
cTFEB;HSACre
LAMP1+ Puncta/ Muscle Section
0.08
*
Males
Females
Controls
cTFEB;HSACre
LAMP1+area (Pixel²)/ Muscle Section
ns
**
I.
Age: 6 Months
Down-regulated
Up-regulated
-log10(qvalue)
log2FoldChange
TFEB
J.
Age: 18 Months
Down-regulated
Up-regulated
-log10(qvalue)
log2FoldChange
TFEB
K.
Ctsb
Lamp1
Ctsl
Psap
Tfeb
Grn
Ctsd
Prkab2
Prkag1
Prkaa2
Lamtor1
Mtor
Lamtor2
Iqgap1
Fkbp3
Prkcq
Hsp90aa1
Mapk14
Eef2
Akt2
Pik3r1
Eif4b
Rps6kb2
Gsk3b
Cdc42
Stat3
L.
Mitochondrial Metabolism
Age-Associated Signaling
Amino Acid Metabolism
Proteostasis
Fatty Acid Metabolism
Overexpressed Protein counts
18 Months
6 Months
Proteasome
HIF-1 signalling pathway
Autophagy-animal
Oxidative phosphorylation
Citrate cycle (TCA cycle)
Pyruvate metabolism
Glyoxylate and dicarboxylate metabolism
2-Oxocarboxylic acid metabolism
Glycolysis/Gluconeogenesis
Starch and sucrose metabolism
Fructose and mannose metabolism
Thermogenesis
Fatty acid metabolism
Fatty acid degradation
Fatty acid biosynthesis
PPAR signalling pathway
Biosynthesis of unsaturated fatty acids
Insulin signalling pathway
AMPK signalling pathway
Glucagon signalling pathway
Longevity regulating pathway
Valine, leucine, and isoleucine degradation
beta-Alanine metabolism
Biosynthesis of amino acids
Tryptophan metabolism
Alanine, aspartate, and glutamate metabolism
Arginine biosynthesis
Arginine and proline metabolism
Lysine degradation
Cysteine and methionine metabolism
M.
Controls
cTFEB;HSACre
kDa
15
10
51
LC3-I
LC3-II
α-tubulin
**
LC3-II/LC3-I Ratio (norm to Tubulin AU)
Controls
cTFEB; HSACre
N.
Hematoxylin/ Eosin
Trichrome
Controls
cTFEB;HSACre
O.
Mstn mRNA Relative Expression (2^-dCT)
*
*
Males
Females
Controls
cTFEB;HSACre
P.
Fndc5 mRNA Relative Expression (2^-dCT)
ns
*
Males
Females
Controls
cTFEB;HSACre

Figure 2

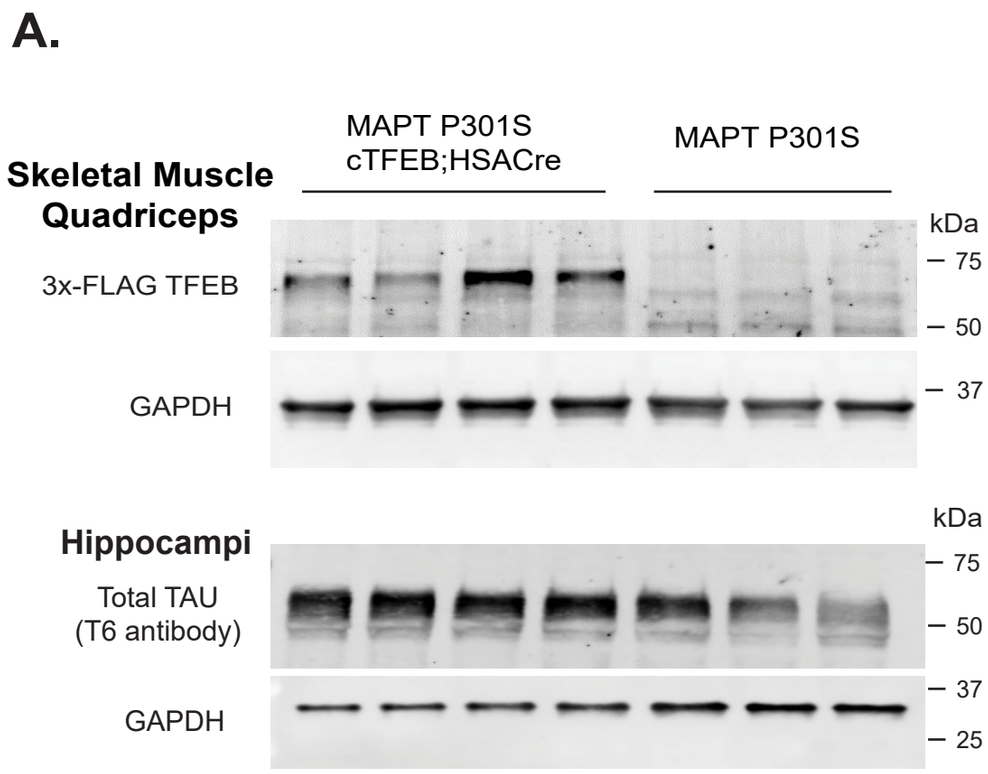
A.
MAPT P301S cTFEB;HSACre
MAPT P301S
Skeletal Muscle Quadriceps
3x-FLAG TFEB
GAPDH
kDa
75
50
37
Hippocampi
Total TAU (T6 antibody)
GAPDH
kDa
75
50
37
25

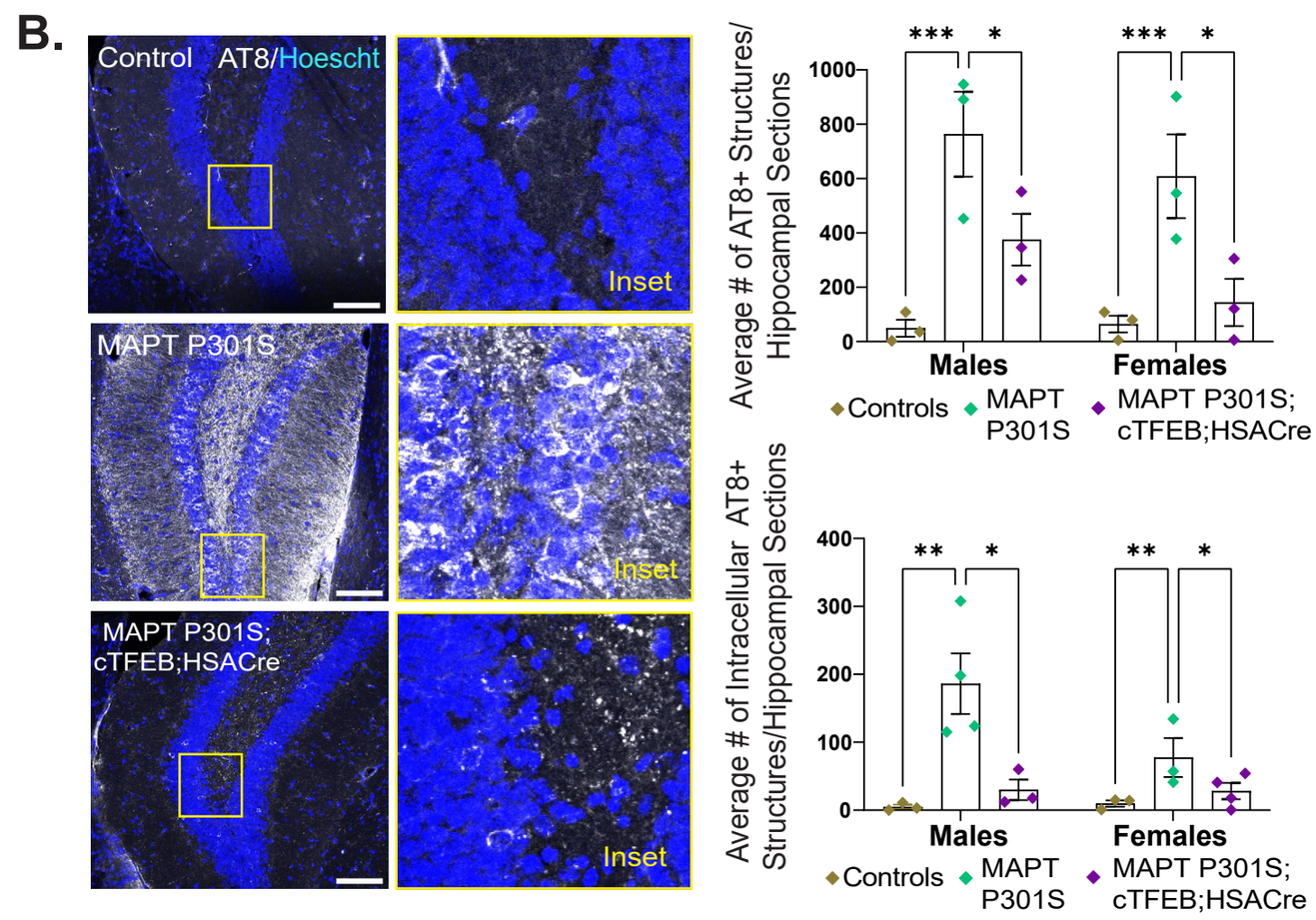
B.
Control
AT8/Hoescht
Inset
MAPT P301S
MAPT P301S; cTFEB;HSACre
Average # of AT8+ Structures/ Hippocampal Sections
Males
Females
Controls
MAPT P301S
MAPT P301S; cTFEB;HSACre
Average # of Intracellular AT8+ Structures/Hippocampal Sections

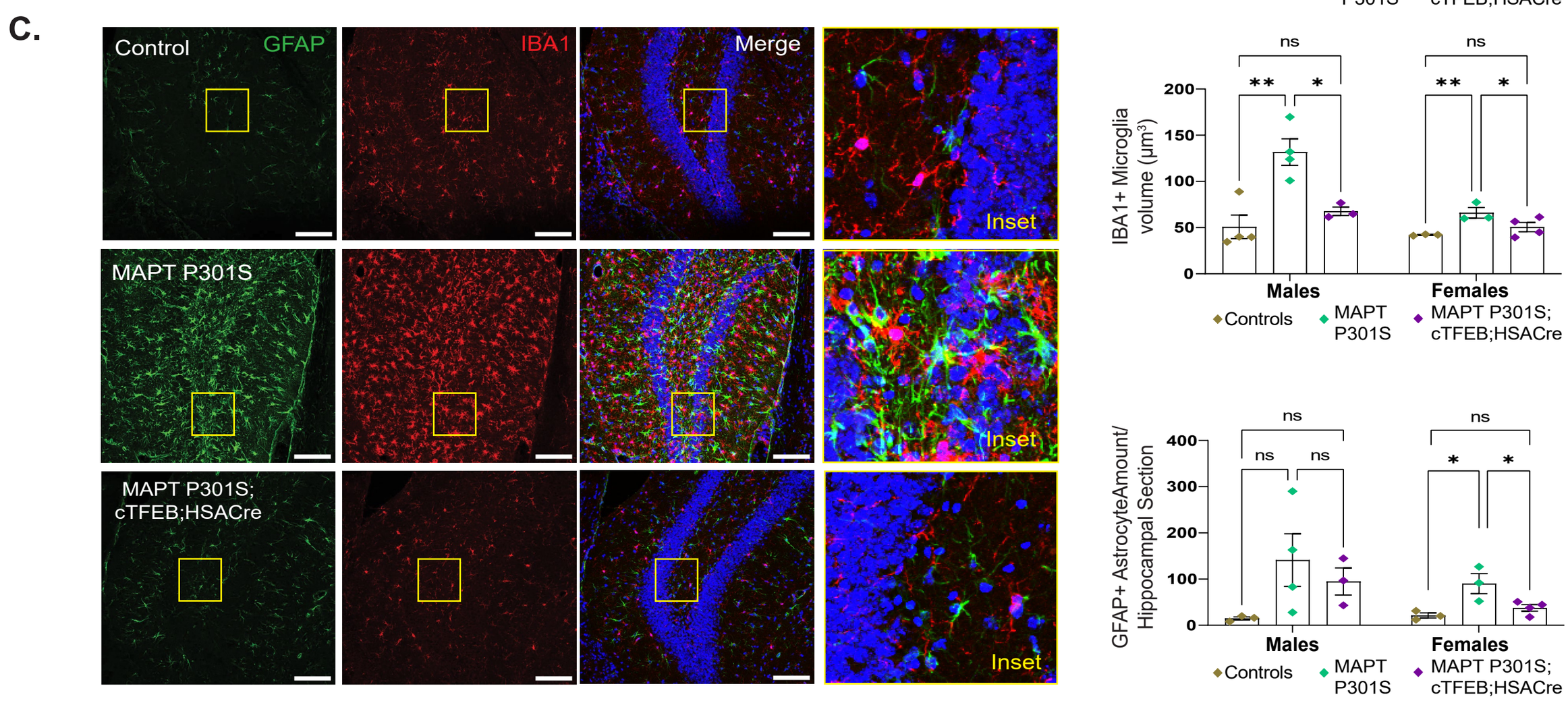
C.
Control
GFAP
IBA1
Merge
Inset
MAPT P301S
MAPT P301S; cTFEB;HSACre
IBA1+ Microglia volume (μm³)
GFAP+ AstrocyteAmount/ Hippocampal Section
ns
Males
Females
Controls
MAPT P301S
MAPT P301S; cTFEB;HSACre

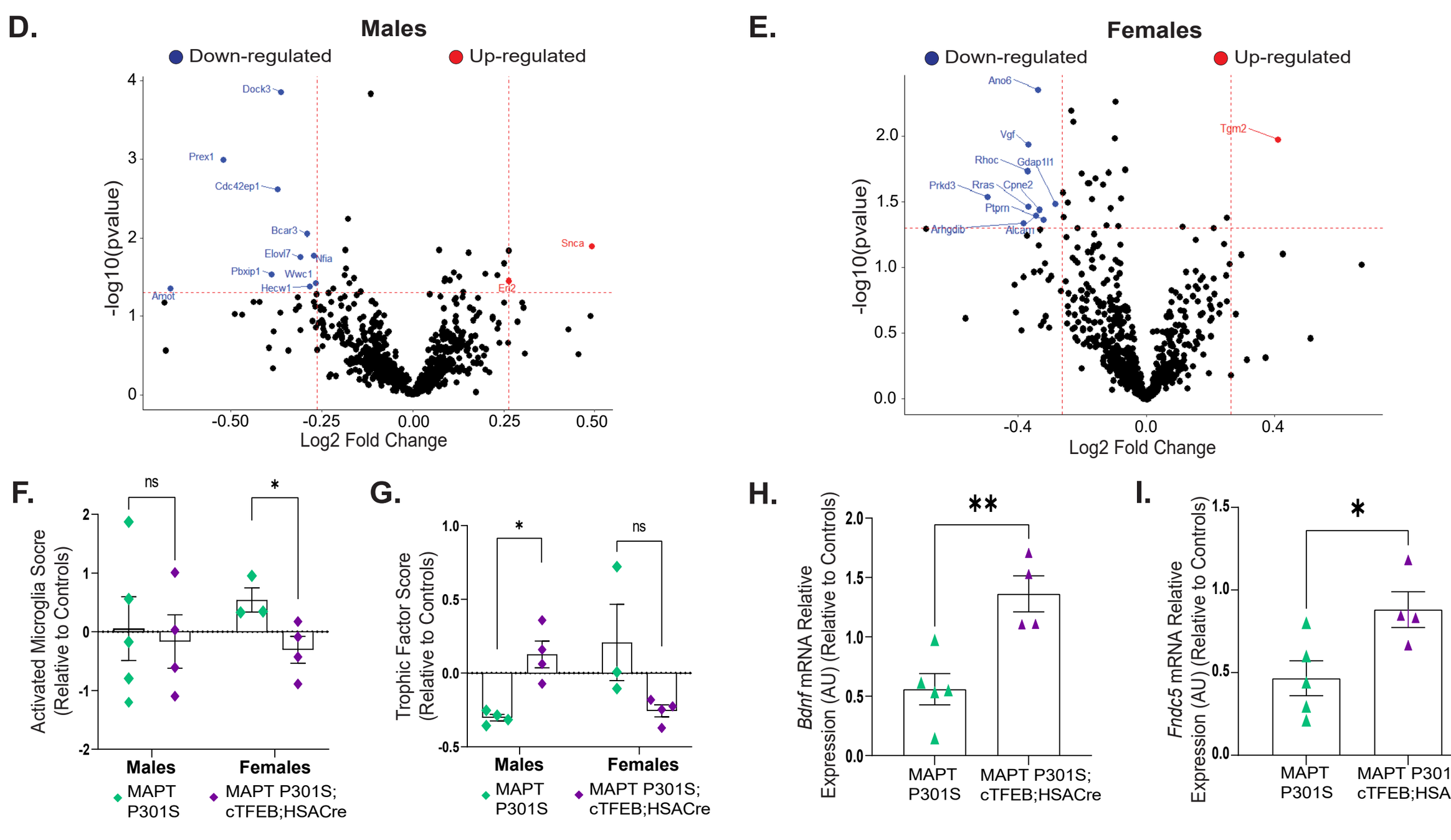
D.
Males
Down-regulated
Up-regulated
Dock3
Prex1
Cdc42ep1
Bcar3
Elovl7
Nfia
Pbxip1
Wwc1
Hecw1
Amot
Snca
Ern2
-log10(pvalue)
Log2 Fold Change
E.
Females
Down-regulated
Up-regulated
Ano6
Vgf
Rhoc
Gdap1l1
Prkd3
Rras
Cpne2
Ptprn
Arhgdib
Alcam
Tgm2
-log10(pvalue)
Log2 Fold Change
F.
Activated Microglia Socre (Relative to Controls)
Males
Females
MAPT P301S
MAPT P301S; cTFEB;HSACre
G.
Trophic Factor Score (Relative to Controls)
Males
Females
MAPT P301S
MAPT P301S; cTFEB;HSACre
H.
Bdnf mRNA Relative Expression (AU) (Relative to Controls)
MAPT P301S
MAPT P301S; cTFEB;HSACre
I.
Fndc5 mRNA Relative Expression (AU) (Relative to Controls)
MAPT P301S
MAPT P301S; cTFEB;HSACre

Figure 3

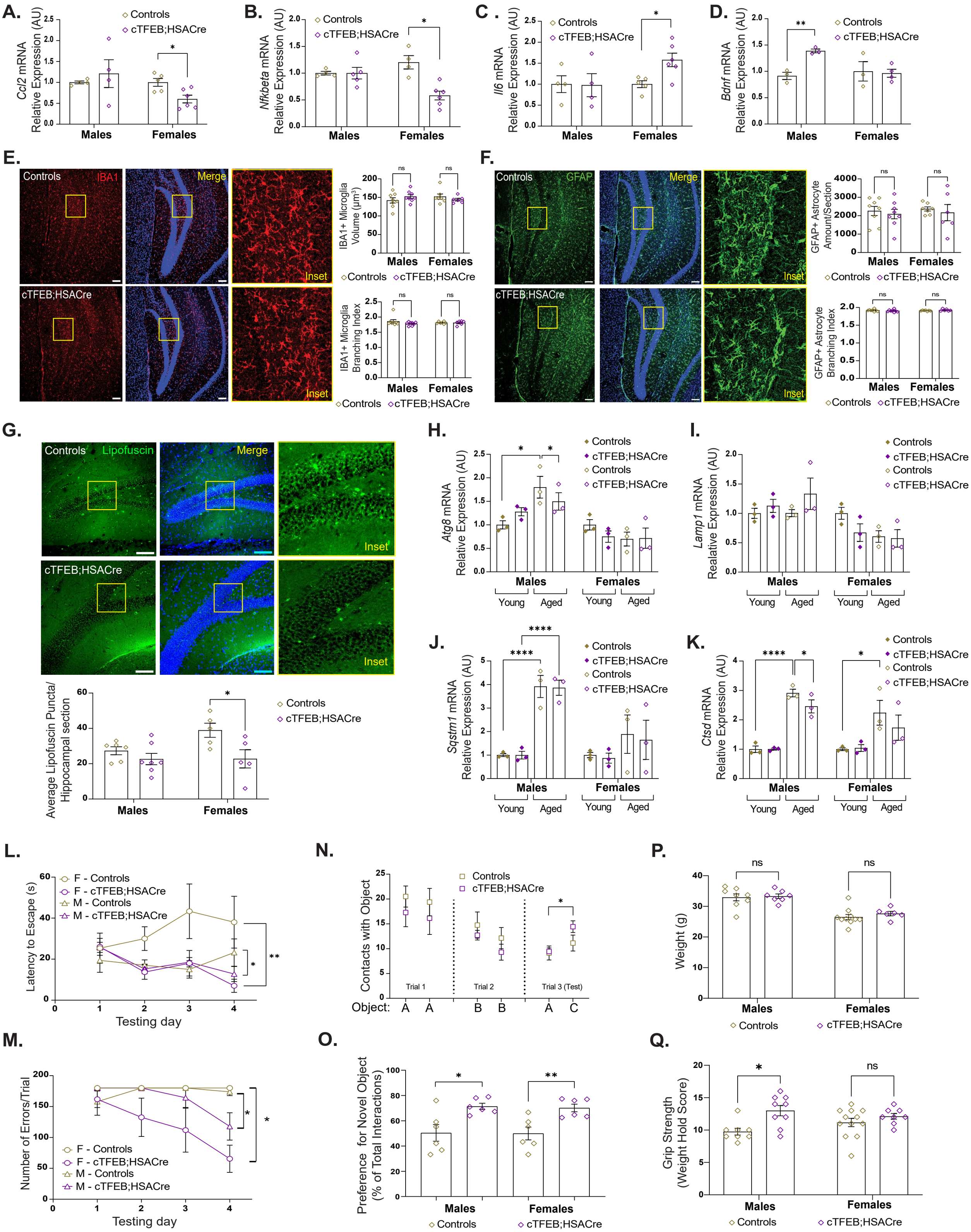
A.
Ccl2 mRNA Relative Expression (AU)
Controls
cTFEB;HSACre
Males
Females
B.
Nfkbeta mRNA Relative Expression (AU)
C.
Il6 mRNA Relative Expression (AU)
D.
Bdnf mRNA Relative Expression (AU)
E.
Controls
IBA1
Merge
Inset
cTFEB;HSACre
IBA1+ Microglia Volume (μm³)
IBA1+ Microglia Branching Index
ns
F.
GFAP
GFAP+ Astrocyte Amount/Section
GFAP+ Astrocyte Branching Index
G.
Lipofuscin
Average Lipofuscin Puncta/ Hippocampal section
H.
Atg8 mRNA Relative Expression (AU)
Young
Aged
I.
Lamp1 mRNA Realative Expression (AU)
J.
Sqstm1 mRNA Relative Expression (AU)
K.
Ctsd mRNA Relative Expression (AU)
L.
F - Controls
F - cTFEB;HSACre
M - Controls
M - cTFEB;HSACre
Latency to Escape (s)
Testing day
N.
Contacts with Object
Trial 1
Trial 2
Trial 3 (Test)
Object: A A B B A C
P.
Weight (g)
Q.
Grip Strength (Weight Hold Score)
M.
Number of Errors/Trial
O.
Preference for Novel Object (% of Total Interactions)

Figure 4

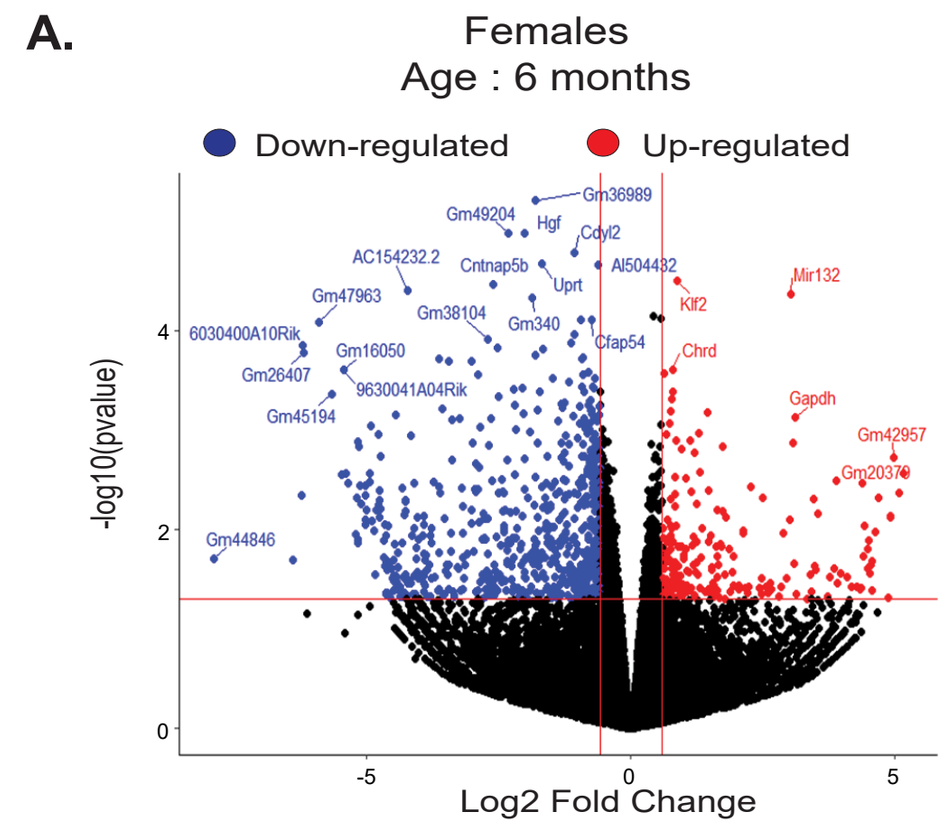
A.
Females
Age : 6 months
Down-regulated
Up-regulated
-log10(pvalue)
Log2 Fold Change
Gm36989
Gm49204
Hgf
Ccyl2
AC154232.2
Cntnap5b
Al504432
Uprt
Gm47963
Gm38104
Gm340
Klf2
Mir132
6030400A10Rik
Gm16050
Cfap54
Chrd
Gm26407
9630041A04Rik
Gm45194
Gapdh
Gm42957
Gm20370
Gm44846

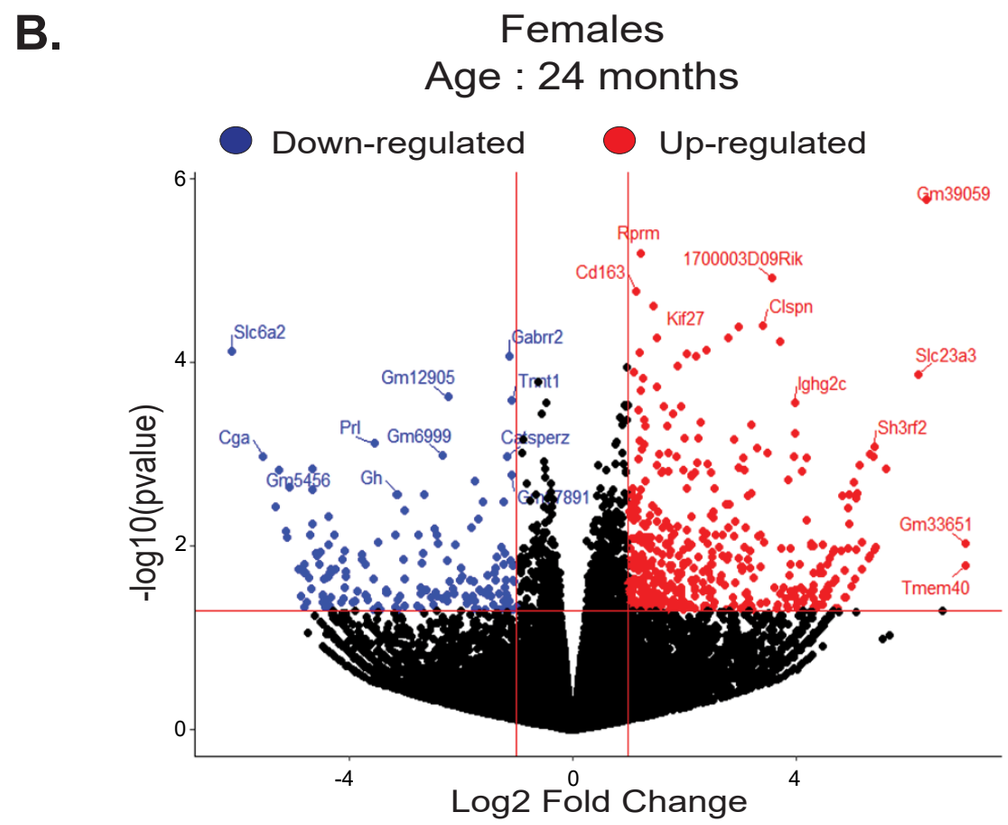
B.
Females
Age : 24 months
Down-regulated
Up-regulated
-log10(pvalue)
Log2 Fold Change
Gm39059
Rprm
1700003D09Rik
Cd163
Kif27
Clspn
Slc6a2
Gabrr2
Slc23a3
Gm12905
Trnt1
Ighg2c
Cga
Prl
Gm6999
Catsperz
Sh3rf2
Gm5456
Gh
Gm17891
Gm33651
Tmem40

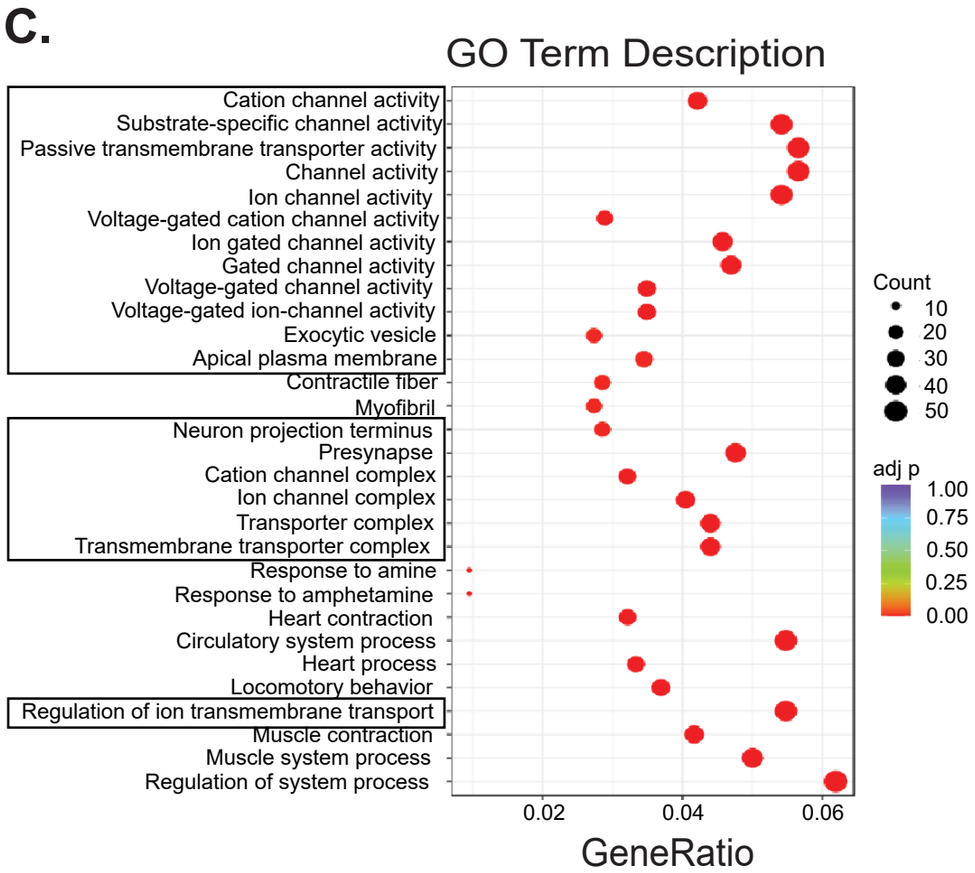
C.
GO Term Description
Cation channel activity
Substrate-specific channel activity
Passive transmembrane transporter activity
Channel activity
Ion channel activity
Voltage-gated cation channel activity
Ion gated channel activity
Gated channel activity
Voltage-gated channel activity
Voltage-gated ion-channel activity
Exocytic vesicle
Apical plasma membrane
Contractile fiber
Myofibril
Neuron projection terminus
Presynapse
Cation channel complex
Ion channel complex
Transporter complex
Transmembrane transporter complex
Response to amine
Response to amphetamine
Heart contraction
Circulatory system process
Heart process
Locomotory behavior
Regulation of ion transmembrane transport
Muscle contraction
Muscle system process
Regulation of system process
Count
adj p
GeneRatio

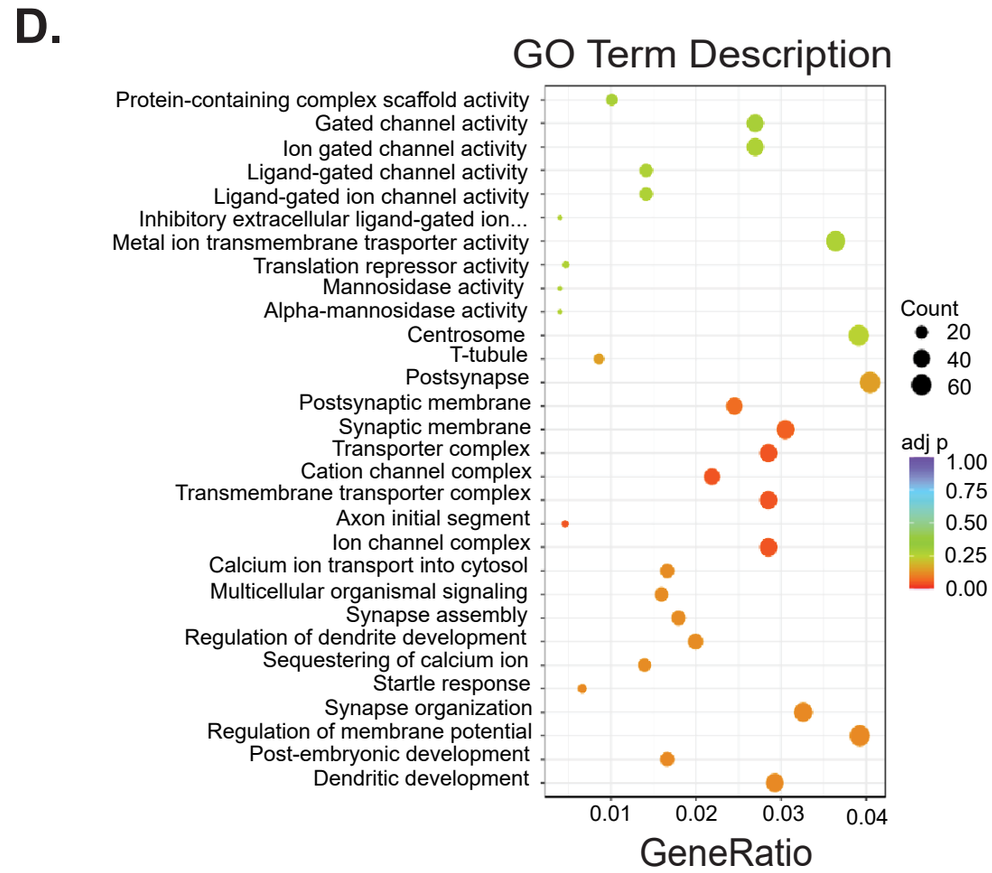
D.
GO Term Description
Protein-containing complex scaffold activity
Gated channel activity
Ion gated channel activity
Ligand-gated channel activity
Ligand-gated ion channel activity
Inhibitory extracellular ligand-gated ion...
Metal ion transmembrane trasporter activity
Translation repressor activity
Mannosidase activity
Alpha-mannosidase activity
Centrosome
T-tubule
Postsynapse
Postsynaptic membrane
Synaptic membrane
Transporter complex
Cation channel complex
Transmembrane transporter complex
Axon initial segment
Ion channel complex
Calcium ion transport into cytosol
Multicellular organismal signaling
Synapse assembly
Regulation of dendrite development
Sequestering of calcium ion
Startle response
Synapse organization
Regulation of membrane potential
Post-embryonic development
Dendritic development
Count
adj p
GeneRatio

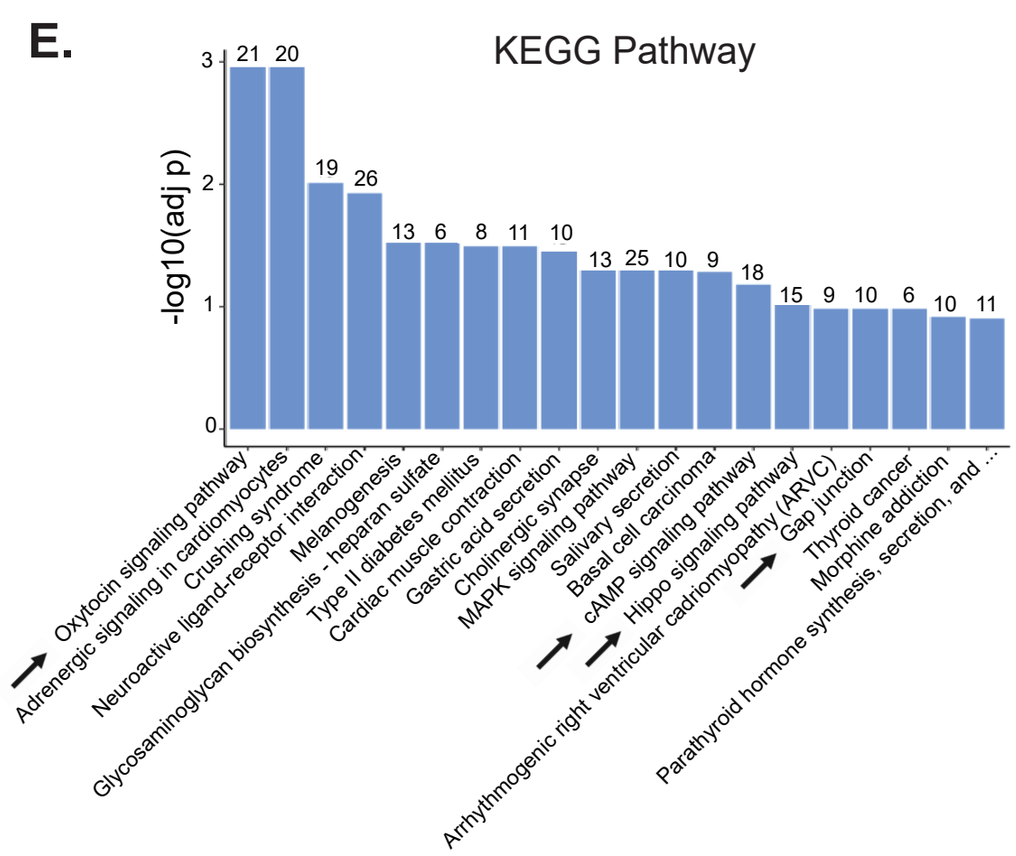
E.
KEGG Pathway
-log10(adj p)
21 20 19 26 13 6 8 11 10 13 25 10 9 18 15 9 10 6 10 11
Oxytocin signaling pathway
Adrenergic signaling in cardiomyocytes
Crushing syndrome
Neuroactive ligand-receptor interaction
Melanogenesis
Glycosaminoglycan biosynthesis - heparan sulfate
Type II diabetes mellitus
Cardiac muscle contraction
Gastric acid secretion
Cholinergic synapse
MAPK signaling pathway
Salivary secretion
Basal cell carcinoma
cAMP signaling pathway
Hippo signaling pathway
Arrhythmogenic right ventricular cadriomyopathy (ARVC)
Gap junction
Thyroid cancer
Morphine addiction
Parathyroid hormone synthesis, secretion, and ...

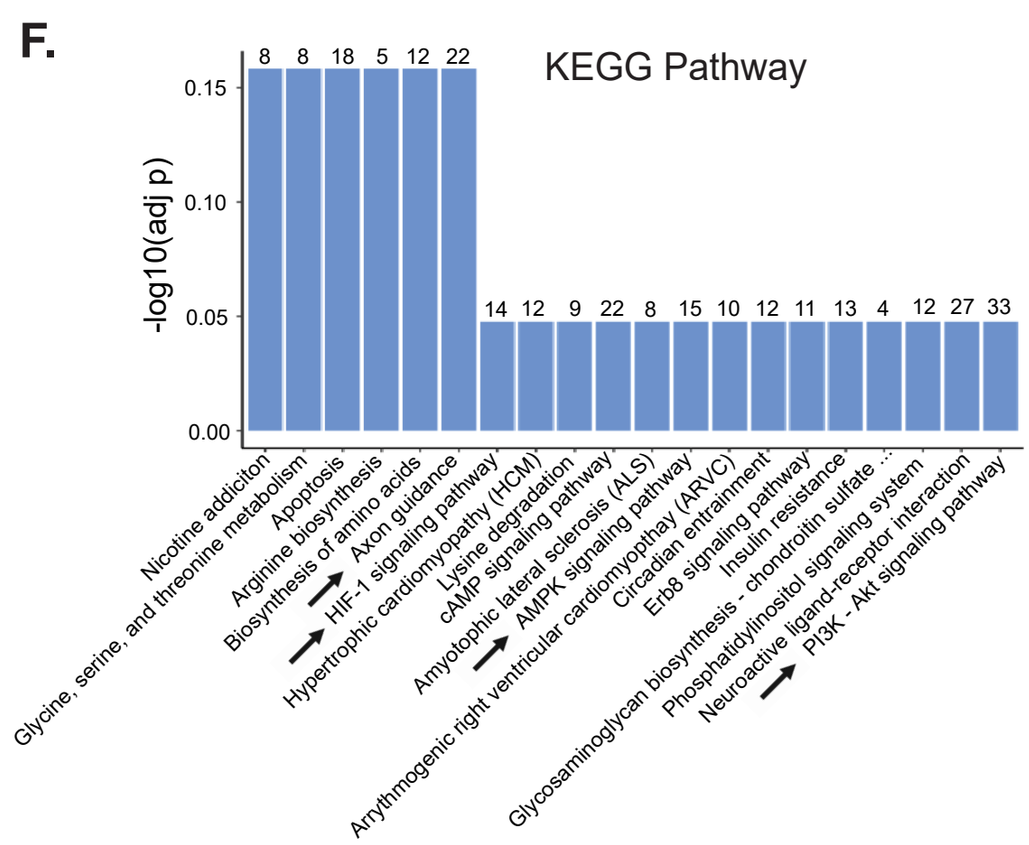
F.
KEGG Pathway
-log10(adj p)
8 8 18 5 12 22 14 12 9 22 8 15 10 12 11 13 4 12 27 33
Nicotine addiciton
Glycine, serine, and threonine metabolism
Apoptosis
Arginine biosynthesis
Biosynthesis of amino acids
Axon guidance
HIF-1 signaling pathway
Hypertrophic cardiomyopathy (HCM)
Lysine degradation
cAMP signaling pathway
Amyotophic lateral sclerosis (ALS)
AMPK signaling pathway
Arrythmogenic right ventricular cardiomyopthay (ARVC)
Circadian entrainment
Erb8 signaling pathway
Insulin resistance
Glycosaminoglycan biosynthesis - chondroitin sulfate ...
Phosphatidylinositol signaling system
Neuroactive ligand-receptor interaction
PI3K - Akt signaling pathway

Figure 5

A.

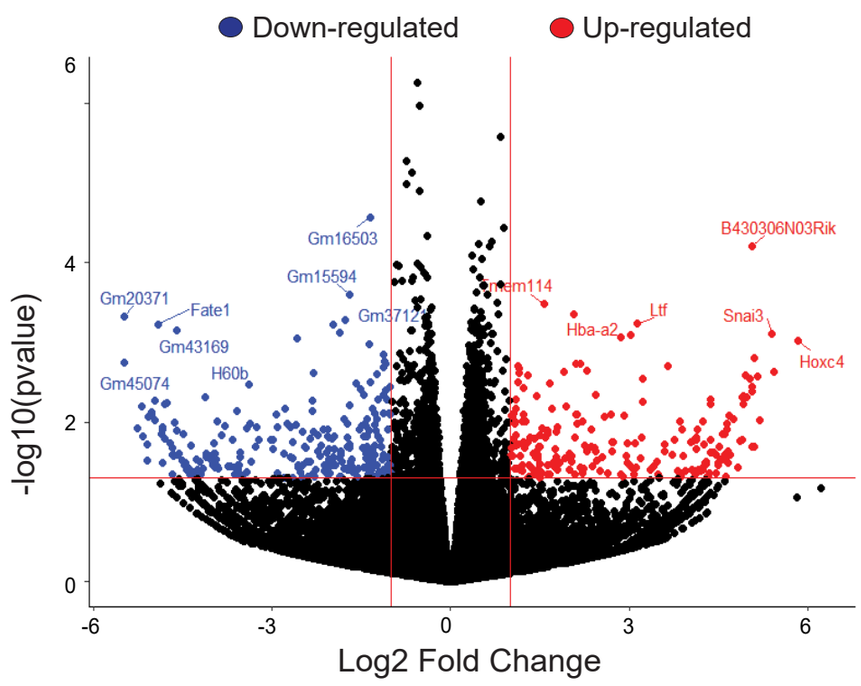

B.

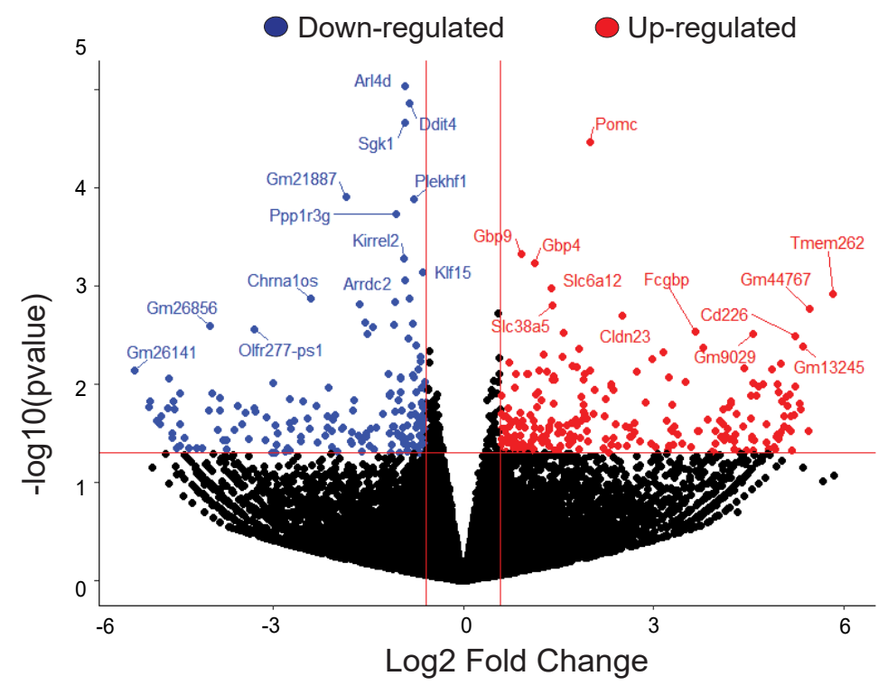

C.

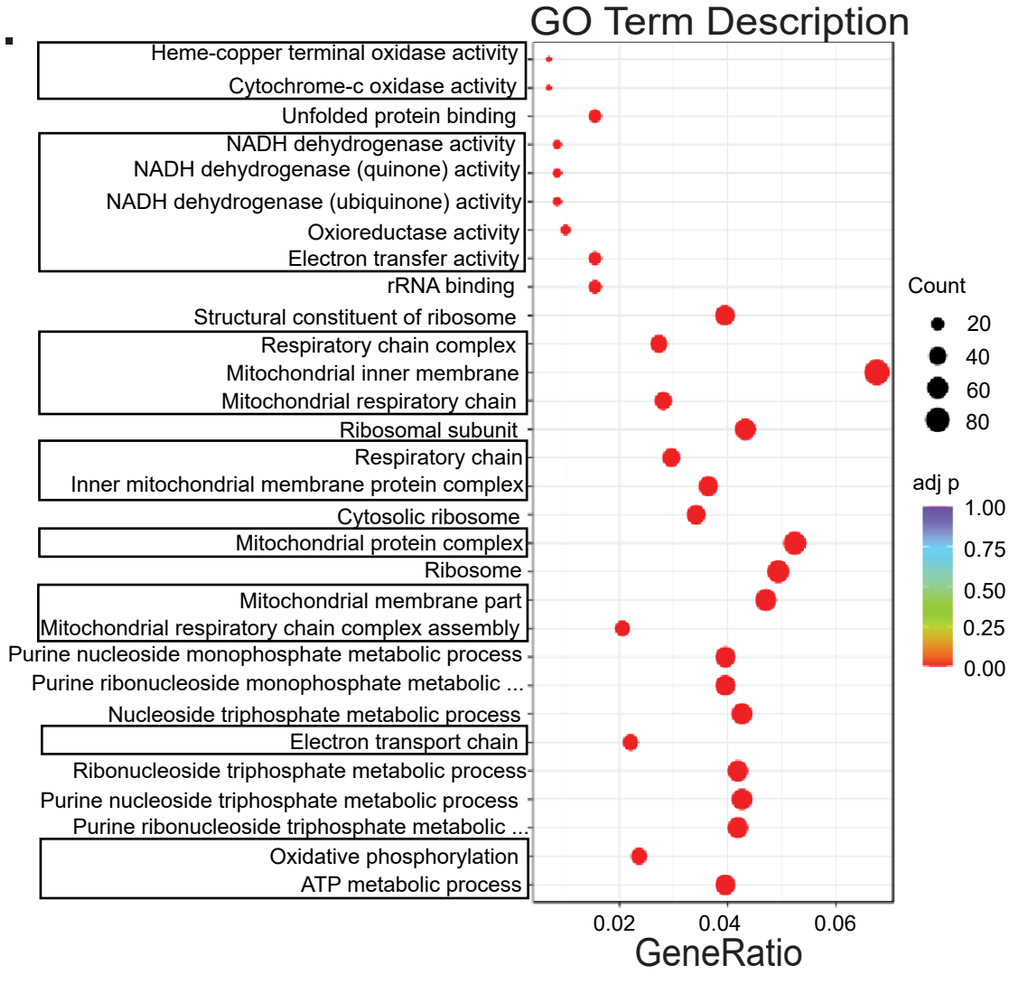

D.

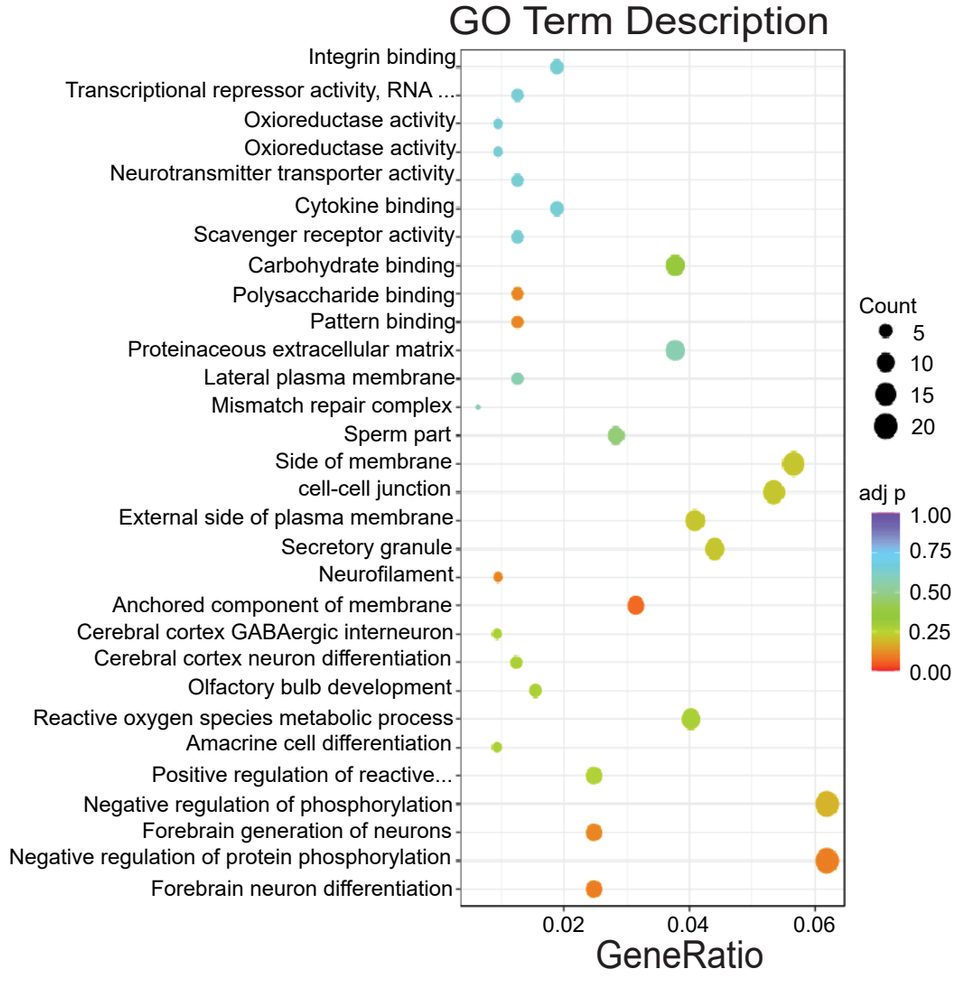

E.

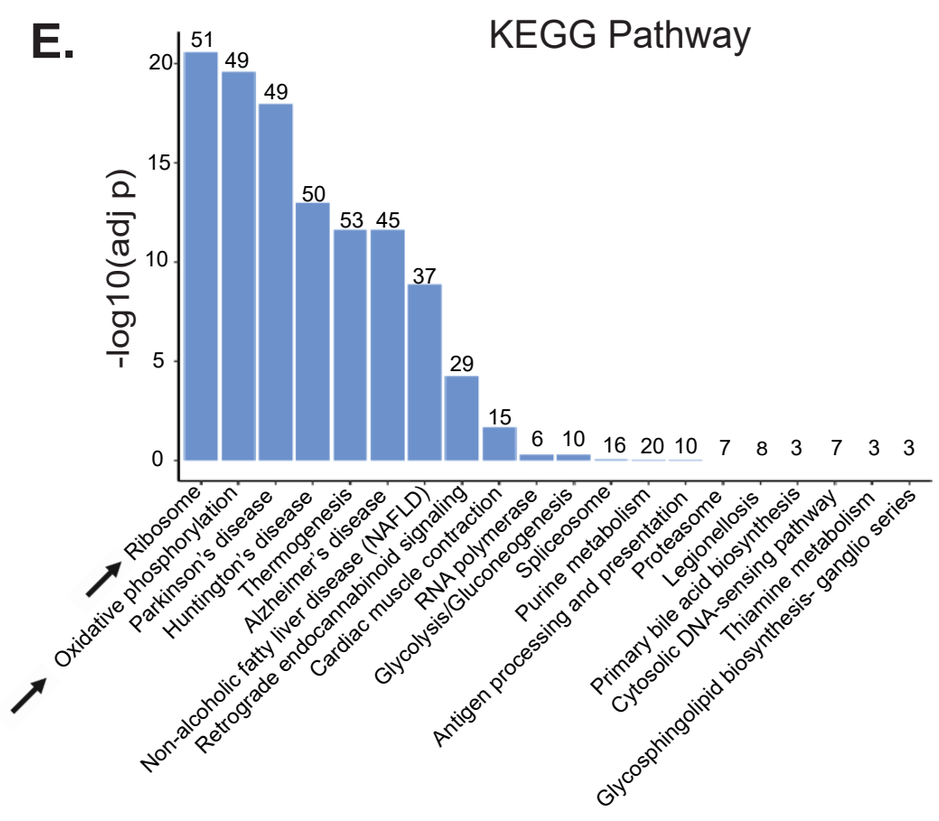
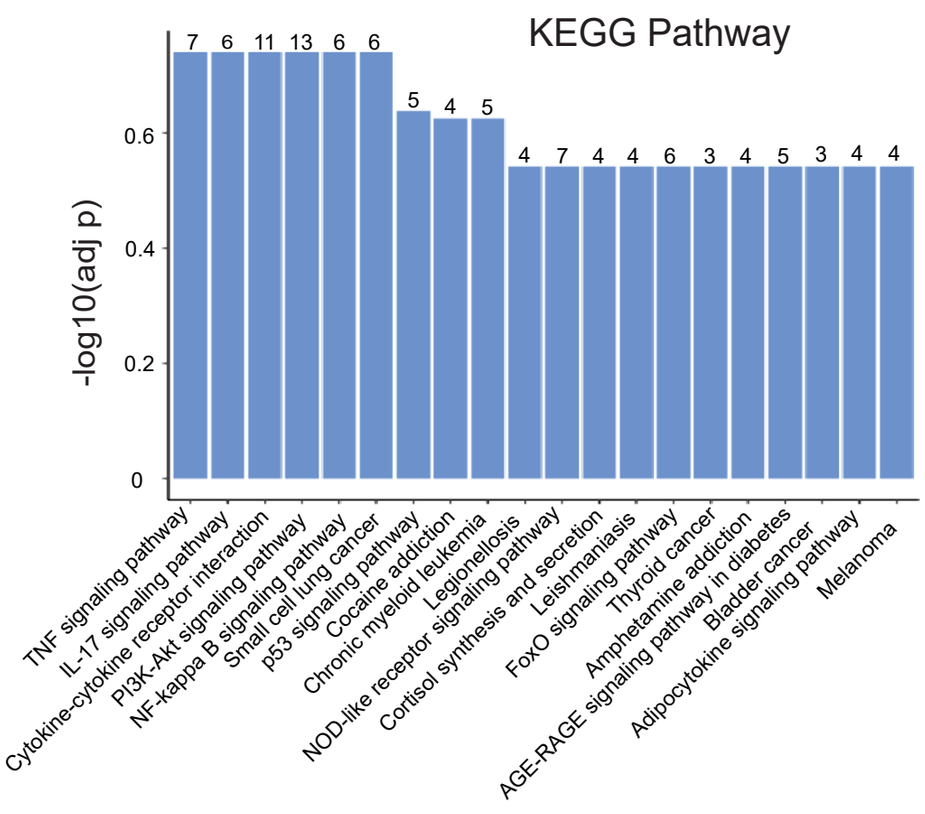
F.